Journal of Materials Chemistry A

ROYAL SOCIETY OF CHEMISTRY

PAPER

View Article Online
View Journal | View Issue

Cite this: J. Mater. Chem. A, 2025, 13, 41122

Tracking phase transformations in $LiMn_{1.5+x}Ni_{0.5-x}O_4$ by high resolution X-ray diffraction

Halvor Høen Hval * and Helmer Fjellvåg*

The stability and structural aspects of three categories of quenched and annealed LMNO samples, representing different stages in the processing of realistic materials, were studied by synchrotron powder X-ray diffraction and Raman spectroscopy. The complex Li–Mn–Ni–O energy landscape opens for coexistence of up to five phases under non-equilibrium conditions. These were evaluated by Rietveld refinements, assisted by lattice parameter – composition correlations, which quantitatively confirmed the nominal bulk composition. Mn/Ni cation diffusion occurs at much lower temperatures (400 °C) than previously anticipated, evidenced by Mn/Ni cation ordering in LMNO and by the (back-)formation of rock salt (o-RS) and N-layered impurity phases. Raman data reveals local Mn/Ni ordering well before the formation of domains detectable by X-ray diffraction. The formation of o-RS and Mn/Ni ordering occurs within the same temperature window. We find that o-RS is most likely the cause for oxygen release, without formation of O-vacancies in the parent spinel. A Mn-enriched e-LMNO spinel phase can form at low temperature alongside the ordering process and back-transformation of Ni-rich impurities. Such Mn/Ni segregations are the main cause of Mn(III) formation in LMNO electrodes. The described procedure provides a basis for detailed analysis of practical LMNO materials, emphasizing that the o-RS phase must be considered an integral part of all such analyses. *Operando* SXRD data further show that ordered and disordered LMNO can be distinguished during cycling, that tetragonal variants form at deep discharge, and that o-RS remains largely undetectable due to its small amount.

Received 24th June 2025
Accepted 27th October 2025

DOI: 10.1039/d5ta05130d

rsc.li/materials-a

Introduction

The ever-increasing worldwide demand for improved performance of rechargeable Li-ion batteries for use in portable electronics, heavy-duty tools and electric vehicles is a strong driver for developing next-generation batteries with high-power and high-energy density based on sustainable materials. In this perspective the well-known spinel $LiMn_{1.5}Ni_{0.5}O_4$ (LMNO) is an appealing cathode material.[1,2] LMNO operates at high voltage (~4.7 V) and has a high achievable specific capacity (~135 mAh g^{-1}) and benefits from more earth abundant elements than conventional $LiCoO_2$ (LCO), $LiNi_{1-x-y}Mn_xCo_yO_2$ (NMC) and $LiNi_{1-x-y}Co_xAl_yO_2$ (NCA).[3,4]

The Ni-substituted LMNO variants of the $LiMn_2O_4$ spinel represents a solid solution of $LiMn_{2-z}Ni_zO_4$ $0.00 \leq z \leq 0.50$ with a tuneable Li-content. The phase relations in the Li–Mn–Ni–O multicomponent system are complex and include spinel and rock salt related phases. For stoichiometric LMNO, an ordered structure ($Li_2Mn_3NiO_8$) is thermodynamically favored at room temperature, ideally with Ni(II) and Mn(IV). Disorder occurs at high temperature, but it is important to emphasize that completely ordered or disordered phases can be hard to obtain in practice,[5,6] and the degree of Mn/Ni order depends on *e.g.* oxygen partial pressure,[7,8] temperature,[9,10] annealing time[6,11,12] and nominal Mn/Ni stoichiometry.[13,14]

The electrochemical performance differs for the ordered and disordered LMNO variants.[15–19] The disordered d-LMNO is (de) lithiated through a solid-solution behavior, as seen in galvanostatic cycling and *operando* diffraction data. Modelling shows that such behavior is possible throughout the whole charge/discharge interval,[20] however, several studies report two-phase behavior at low Li-contents.[21,22] The ordered o-LMNO (de)lithiates as three distinct spinel phases (approximately $LiMn_{1.5}Ni_{0.5}O_4$, $Li_{0.5}Mn_{1.5}Ni_{0.5}O_4$ and $Mn_{1.5}Ni_{0.5}O_4$), with two-phase equilibria during electrochemical cycling. These o-LMNO variants exhibit a limited solid-solution behavior at the two-phase boundaries during charge/discharge.[20,23] Relative to o-LMNO, d-LMNO is reported to show improved electrochemical stability at high voltage[9,24,25] with less degradation and capacity fading.[6,13,26] It has been reported that d-LMNO has a higher electronic conductivity,[27] although several studies dispute that claim.[6,28,29] An improved rate capability[6,28] is reported for d-LMNO and explained by higher ionic conductivity,[30] however;

Centre for Materials Science and Nanotechnology, Department of Chemistry, University of Oslo, P. O. Box 1033 Blindern, N-0315 Oslo, Norway. E-mail: h.h.hval@kjemi.uio.no; helmerf@kjemi.uio.no

recent reports show comparable rate capabilities across the two polymorphs,[7] except for highly ordered o-LMNO.[6,28]

The complex energy landscape in the Li–Mn–Ni–O system is an issue both for synthesis and electrochemistry. The complexity is likely rooted in similarities in the atomic arrangements, with a cubic close packed O-anion sublattice where cations may fill various tetrahedral and octahedral interstices. The similar synthesis conditions of o-LMNO and d-LMNO has been theoretically understood from DFT-calculations showing how the similar characteristics of Ni–O and Mn–O bonds leads to small differences in lattice enthalpy[31] and others have shown how disorder come from intrinsic defects in o-LMNO, which are highly sensitive to synthesis conditions.[32] Furthermore, depending on temperature (T) and oxygen partial pressures (pO_2), different oxidation states for Mn and Ni can be stabilized. One consequence is that thermal decomposition of LMNO may take place (high T, low pO_2) under formation of a Ni-rich rock salt phase. Several reports suggest presence of oxygen vacancies in the spinel,[9,13,33,34] but many neutron diffraction studies do not report vacancies.[9,35–38] Notably, the reported formation of (microscopic) Ni-rich rock salt type precipitates[35,38,39] may instead explain any oxygen release. The decomposition reactions are detrimental for performance in a Li-ion battery, with capacity loss caused by Li fixation in impurities and a possible nickel accumulation in the surfaces of crystallites, that could cause overpotentials and harm conductivity.[35] Any reduction in the electrochemical cell energy due to a decreased amount of electroactive Ni, as well as more Mn(III) that can undergo disproportionation and induce decomposition reactions on the anode, is detrimental for the electrochemical cell performance.[40]

Since the X-ray scattering contrast between Mn and Ni is poor, and Li is a weak scatterer, one can hardly extract reliable composition data from Rietveld refinements of site occupancies. However, excellent signal-to-noise ratio and high-resolution synchrotron X-ray diffraction (SXRD) allows us to identify (i) Mn/Ni (dis)ordered domains and (ii) tiny amounts of impurity phases, in addition to (iii) resolve overlapping peaks from related compounds. This enables determination of unit cell dimensions with good accuracy and allows us to establish and benefit from volume–composition relationships. This was previously adopted for the rock salt (RS) impurity described by McCalla *et al.*, with (partial) cation ordering and Li-substitution into an $MnNi_6O_8$-like phase[41] (with a diffraction pattern similar to that of $Li_xNi_{1-x}O$).[42] To complement this analysis, other methods such as powder neutron diffraction (ND),[9,36,37,43] Nuclear Magnetic Resonance (NMR),[35] Raman[22,43,44] and Fourier-Transform Infrared (FTIR)[27] spectroscopy are valuable in phase identification and to identify space group and local symmetry. In the current work, the SRXD study is complemented by Raman spectroscopy.

The Mn/Ni ordering process as well as the RS segregation rely on cation diffusion within the spinel structure, facilitated by empty tetrahedral and octahedral sites. At the atomic scale, the mechanism for Mn/Ni ordering is proposed[13,45] to involve Frenkel-type defects where Mn/Ni atoms in 16d sites are temporarily shifted to empty 16c sites. Such shifts are believed to be central also for formation of RS impurities, accompanied by Li movement to octahedral sites, redox processes and oxygen release.[13]

The fully ordered and fully disordered LMNO represent two extreme situations. TEM data show that ordered and disordered domains can coexist at the atomic level and the domains of o-LMNO are believed to randomly form and grow inside disordered d-LMNO crystallites.[46] Tiny clusters of o-LMNO are detectable by Raman spectroscopy owing to a different local symmetry. The nanosized domains inside LMNO crystallites will give rise to very broad diffraction peaks, easily hidden in background noise. The SXRD patterns will show sharp peaks from the spinel structure, and broad peaks from the ordered domains. A few reports have described such coexistence based on either powder diffraction data[47–50] or electrochemistry.[13] Emery *et al.* reported domains of just a few nm in size for LMNO prepared at 900 °C.[14] The detection of such tiny domains can easily be overlooked, which could lead to erroneous correlations between ordering and properties.

This work makes use of high-intensity and high-resolution synchrotron X-ray diffraction to address open issues with spinel stability, ordering of domains, and segregation, based on a systematic study of some 80 samples of $LiMn_{1.5+x}Ni_{0.5-x}O_4$ (x = 0, 0.05, 0.1). One question is how ordering correlates with (rock salt) impurities. Already for the disordered spinel, short-range order is likely present as a required means for charge neutrality. During the domain growth, these may join with possible formation of antiphase boundaries (APBs).[15,16,51] These may act as traps for charge carriers, *cf.* $La_{2/3-x}Li_{3x}TiO_3$.[20] One should hence aim to engineer an optimum ordering and microstructure for best electrochemical performance. We explore the temperature range where the o-RS formation can be mitigated/reversed, and Ni/Mn ordering occurs to gain insight to these interconnected phenomena. This includes study of how the Mn/Ni ratio affects underlying mechanisms. Our efforts are based on three categories of samples: (i) those with maximum Mn/Ni order, (ii) those quenched from a high temperature disordered state and (iii) quenched with subsequent annealing. These samples span a processing range that is relevant as a basis for synthesis and optimization of commercial LMNO. The correlation between ordering and formation of impurities and segregation is discussed in detail. Finally, we propose a synthesis route for minimizing the amount of impurities in the final product, depending on the Mn/Ni stoichiometry.

Experimental

Synthesis

Powder samples of $LiMn_{1.5+x}Ni_{0.5-x}O_4$ (x = 0.00, 0.05, 0.10, 0.20, 0.30, 0.40) were prepared by a modified Pechini method,[52] where ethylene glycol (EG, 99.8%, Sigma-Aldrich) and citric acid monohydrate (CA, 99.0%, Sigma-Aldrich) are mixed in a 4 : 1 molar ratio.[21,43] Large batches (18 grams; 0.1 mol) were prepared by first mixing anhydrous $LiNO_3$ (99.999%, Alfa Aesar) with standard solutions of 0.884(2) mmol per g $Ni(NO_3)_2$ (from 98.5% $Ni(NO_3)_2 \cdot 6H_2O$, Sigma-Aldrich) and 3.023(8) mmol per g $Mn(NO_3)_2$ (from 98% $Mn(NO_3)_2 \cdot 4H_2O$, Supelco) based on

gravimetric analysis. Next, EG and CA were added, stirred overnight at 50 °C, and heated to 120 °C to remove water. On increasing the temperature to 220 °C the sample self-ignited and was kept overnight in a muffle furnace at 180 °C. Organic components were next decomposed at 400 °C for 4 h. A final treatment was done at 900 °C for 10 h followed by cooling to 800 °C and holding for 10 h. The samples were mildly quenched by letting the samples cool in ambient air. These quenched samples were used as starting material for all annealed samples. The adopted notation describes the Mn stoichiometry, followed by *Q* for quenched. Thus, Mn1.55-*Q* describes a quenched sample with stoichiometry $LiMn_{1.55}Ni_{0.45}O_4$. Portions of the Mn1.5-*Q*, Mn1.55-*Q* and Mn1.6-*Q* samples were subsequently annealed for 6 h, at selected temperatures (400–750 °C) and atmospheres (static air or O_2-flow). Details are defined by the shorthand notation: *e.g.* Mn1.55-O2-500C is annealed in O_2-flow at 500 °C. A few samples were prepared by slow cooling during 18 d from 725 to 400 °C (details in Table S1) to maximize the degree of Mn/Ni cation order. These are named MO, for maximum order: Mn1.5-MO, Mn1.55-MO, Mn1.6-MO. The stoichiometry of the MO samples was confirmed by ICP-OES to be very close to the nominal values, *i.e.* $Li_{0.98}Mn_{1.496}Ni_{0.504}O_4$, $Li_{0.98}Mn_{1.551}Ni_{0.449}O_4$ and $Li_{0.99}Mn_{1.599}Ni_{0.401}O_4$.

Powder X-ray diffraction

Synchrotron powder X-ray diffraction data (SXRD) were collected at ambient conditions at SNBL, BM01@ESRF, Grenoble. To compare the data, collected at slightly different wavelengths, the observed profiles are presented as a function of *Q* rather than 2θ. During the campaigns different sample-to-detector distances were applied which allowed us to collect data for a very broad *Q*-range, and notably also for a smaller *Q*-range with superior resolution. An overview is given in Table S2, for angular resolution, wavelength and counting time. The choice of *Q*-range has an impact on the outcome of Rietveld refinements, especially in terms of domain and crystallite sizes. Details regarding which samples were measured under which conditions as well as the goodness of fit for each diffractogram are shown in Fig. S1. All samples were kept in 0.3 mm borosilicate capillaries, and a Pilatus 2M detector was used. To integrate the 2D-data, we used the Bubble software.[53] The detector was calibrated using a LaB_6 standard (NIST Standard Reference Material 660c), adopting an intrinsic peak broadening function for the 2D detector.[54] *Operando* SXRD studies by cycling 1.5–5.0 V (C/8) were done at SNBL, BM31@ESRF, as described in Table S11. Further description of methodology and instrumentation is published previously.[55]

Structure analyses

Up to six phases were included in the structural analyses, see Table S3 for crystallographic data. These include: the Mn/Ni disordered LMNO (d-LMNO) described in space group $Fd\bar{3}m$ with Li in 8a (1/8, 1/8, 1/8); Mn/Ni in 16d (1/2, 1/2, 1/2); O in 32e (*x*, *x*, *x*); the expanded spinel (e-LMNO), similar to d-LMNO but with a prominent Li and Mn/Ni mixing; the Mn/Ni ordered LMNO (o-LMNO) described in space group $P4_332$; Li in 8c (*x*, *y*, *z*), Mn in 12d (*x*, *y*, *z*), Ni in 4a (*x*, *y*, *z*), O1 in 8c (*x*, *y*, *z*); O2 in 24e (*x*, *y*, *z*); the ordered rock salt phase (o-RS), literature composition $MnNi_6O_8$, described in $Fm\bar{3}m$, with Mn in 4a (0, 0, 0), Ni in 24d (0, 1/4, 1/4), O1 in 8c (1/4, 1/4, 1/4), O2 in 24e (*x*, 0, 0), where the 4b site (1/2, 1/2, 1/2) is vacant, but can accommodate Li; the layered rock salt-related phase (N-layered) described in $R\bar{3}m$, with predominantly Mn/Ni in 3a (0, 0, 0) and mainly Li in 3b (0, 0, 1/2), but cation mixing occurs, and O in 6c (*x*, 0, 0). A similar description is adopted for the M-layered phase, thus ignoring superlattice peaks that can be indexed in the *C*2/*m* space group.[56] For the analysis of low voltage behaviour, the tetragonally distorted Li-rich phases T1 and T2 were included, both space group $I4_1/amd$. T1 is refined as L_2MNO ($Li_2Mn_{1.5}Ni_{0.5}O_4$), with Li in 8c (0, 0, 0), Ni and Mn in 8d (0, 0, 1/2) and O in 16 h (0, *y*, *z*). T2 is more Li rich, ($Li_{2.5}Mn_{1.5}Ni_{0.5}O_4$), and here Li occupies also the 4a-site (0, 3/4, 1/8), see Jobst *et al.*[57]

Rietveld refinements

All profile and Rietveld refinements were performed using TOPAS v6 (Bruker AXS). The background was modelled as a polynomial of 7th degree. For the largest *Q*-range data, additional corrections were introduced as three very broad peaks; one at $Q = 1.5$ Å^{-1} to account for an amorphous signal from the capillary, and two at $Q = 4.76$ Å^{-1} and 6.77 Å^{-1} to account for a sinusoidal shape of the background. In refinements combining data sets for two detector positions, a weighting of 9-to-1 in favour of the superior resolution position was applied. This led to similar R_{wp}-values for both detector positions (weighting $1/Y_{obs}$). Details on structural and thermal parameters, Bragg reflections and fitted parameters are given in Table S3. Distance restraints based on reported bond-lengths[58,59] were applied to help assuring realistic values for certain site occupancies and atomic positions. Details are given in Tables S4 and S5. The reported errors throughout this work refer to the e.s.d. values obtained from Topas multiplied by a factor of three, thus representing probable errors (e.p.e.), see Bérar *et al.*[60]

Methodology for evaluating Mn/Ni ordering

The global (local) Mn/Ni ordering is evidenced by additional, often broad, diffraction peaks due to symmetry lowering and particle size, as well as by additional modes observed by Raman spectroscopy. Upon ordering, the symmetry is lowered from $Fd\bar{3}m$ to $P4_332$, which gives rise to superstructure peaks with mixed parity of *h*, *k* and *l* (*i.e.* not all odd, or not all even). Owing to the poor X-ray scattering contrast between Mn and Ni cations, a proper characterization requires synchrotron radiation and use of 2D-detectors. Experimentally, the superstructure peaks are broader than the characteristic peaks of the spinel phase. This is due to the microstructure where the ordered domains are significantly smaller than the crystallite size.[15]

The width (FWHM) of the (*hkl*) superstructure peaks is described in eqn (1) by a Lorentzian broadening, Lor_{FWHM}:

$$Lor_{FWHM} = \frac{\lambda}{\cos(\theta) \times \xi} \quad (1)$$

$$D_0 = \pi^* K/\xi \quad (2)$$

where ξ is the correlation length of the ordered domains, λ the wavelength and θ refers to the (hkl) peak position. ξ correlates to the domain size, D_0, through eqn (2), where K is a dimensionless constant set to 0.94 as conventionally done when using Scherrer's formula.

The intensity of the superstructure peaks cannot be explained by the moderate difference in Mn/Ni X-ray scattering power and ordering of Mn and Ni at 12d and 4a sites. In fact, our analysis shows that the main contribution to the intensity stems from atomic displacements owing to the differently sized and ordered Ni(II) and Mn(IV) cations. Hence, these peaks are indirectly a measure of ordering.

In this situation, we quantify the degree of Mn/Ni ordering by comparing intensities of superstructure peaks relative to peaks from the regular spinel-type structure, specifically, the ratio between the (310) ordering peak and the (222) spinel peak. These are chosen as (310) is a prominent ordering peak and (222) occurs at a similar Q value and is not influenced by any transition metals on Li sites as is the case for (311). This ratio we define as the relative ordering (RO), as shown in eqn (3). The peak intensities are determined analytically as described in Table S6.

$$\mathrm{RO} = \frac{I_{(310)}}{I_{(222)}} \quad (3)$$

Owing to the broadening, domains of a certain size are needed for the quantification. Care should be taken, since RO is thus not only a measure on the degree of ordering, but also correlates with the size of the domains, and may furthermore be affected by instrument resolution and impurity phases during the profile/Rietveld fitting. Due to this the RO is not a measure to quantify the distribution of Ni and Mn in the 4a/12d sites, but rather a measure of the ordering in the sample overall – thus correlating with the relative amount of o-LMNO compared to the total amount of LMNO (both ordered and disordered).

Raman spectroscopy

Data were collected with a Renishaw inVia, instrument (Aarhus University) using a green 514 nm Ar-ion laser with a grating of 1200 l mm^{-1}. Using a ×50 objective, the lateral resolution is ~1 μm, and the spectral resolution is ~1 cm^{-1}. Multiple sets of data were collected to remove outliers due to poor focus. At least three spots were probed on each sample, and for most samples only the measurement with the most prominent ordering signatures is reported in this work. We provide examples of spots showing different degree of order, to highlight the variations observed.

Results

Benchmarking-model samples

Three categories of LMNO samples were examined; samples (i) subjected to long term annealing at moderate temperatures to maximize ordering (MO) of Mn/Ni cations; (ii) quenched (Q) from 800 °C, which represents the starting point for all samples subjected to post-annealing; (iii) quenched and post-annealed under temperatures and pO_2 relevant to study the structural features and imperfections present in real LMNO samples. A multitude of structurally related phases occur in these synthesized materials, dependent on the conditions.

Identification of spinel phases from XRD data

Up to at least five phases may exist in Li–Mn–Ni–O samples with nominal compositions relevant for LMNO spinel synthesis. We first describe how these phases are conveniently identified based on high resolution SXRD data. Concrete examples from Mn1.6-500C are included.

The main spinel phases; disordered (d) and ordered (o) LMNO

d-LMNO. Characteristic spinel peaks according to space group $Fd\bar{3}m$ (Fig. 1a). Lattice parameters 8.17–8.21 Å, depending on Mn/Ni stoichiometry. May exhibit a small degree of inversion with minor amounts of Mn/Ni in tetrahedral sites,[61] evidenced by increased peak intensity of certain reflections, especially (220) at around Q = 2.17 Å^{-1}, but also (422), (620) and (642) shows a similar variation in high-quality diffraction data.

o-LMNO. In addition to characteristic $Fd\bar{3}m$ peaks, weak superstructure peaks are observed (marked by "+" in Fig. 1a). A high-intensity X-ray source is required. The most prominent ordering peaks are (310), (320) and (410), around Q = 2.44 Å^{-1}, 2.78 Å^{-1} and 3.18 Å^{-1}, respectively. The ordering peaks are broader due to small domain size of ordered regions and may be hard or impossible to detect for very small domains, depending on data quality. The data and peak fitting should be visually inspected, as very small domains may easily drown in the background.

Co-existence of d-LMNO/o-LMNO. This situation is most prominent for Mn-rich samples, where the lattice parameter of d-LMNO becomes significantly larger than for o-LMNO, but Mn1.5-samples can also show sign of phase coexistence. The most apparent sign of o-LMNO is not necessarily the superstructure peaks (which can be very hard to detect), but rather asymmetric peak shapes of the spinel $Fd\bar{3}m$ peaks. High-resolution data is normally required. An example of unravelling the coexistence of d-LMNO and o-LMNO is shown in Fig. S3–S5.

Identification of impurity phases (o-RS, e-LMNO, N-layered RS)

o-RS (ordered RS). In some cases, the simple NiO rock salt (RS) structure is sufficient for describing the rock salt impurity phase (marked by "*" in Fig. 1a). However, in high-quality data, as presented in this work, most samples show additional peaks due to Mn/Ni ordering corresponding to a partially cation-deficient $MnNi_6O_8$-like structure, o-RS. The phase is recognized by (222) and (400) at around Q = 2.62 Å^{-1} and 3.02 Å^{-1}, corresponding to (111) and (200) for the simple rock salt. This phase has a large a-axis (a = 8.27–8.32 Å), which makes it easy to

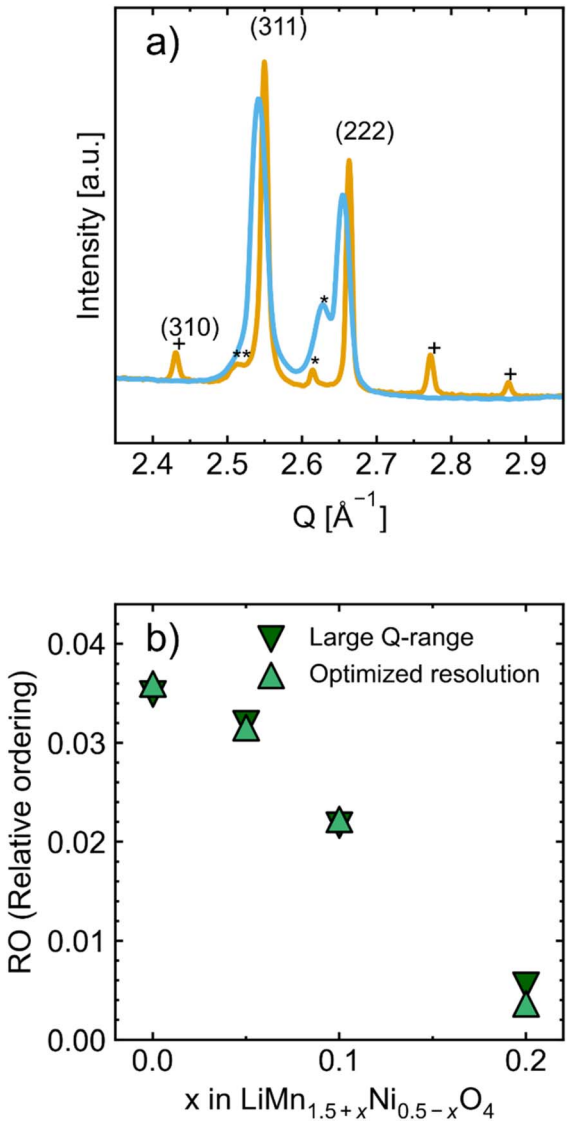

Fig. 1 Powder X-ray diffractograms for Mn1.5; (a) comparison of a disordered sample (Mn1.5-*Q*, blue), heated at 800 °C and quenched (*Q*) and a maximum ordered sample (Mn1.5-MO, orange), cooled very slowly in O_2-flow. Logarithmic intensities are used to highlight low-intensity peaks. In addition to the characteristic (311) and (222) from the spinel, diffraction peaks due to Mn/Ni ordering, including (310) (+), rock salt impurities (*) and an expanded spinel impurity e-LMNO (**) are visible, see text below; (b) calculated intensity ratio according to eqn (3) for MO-samples, showing variation in the relative ordering (RO), calculated from data collected at the two different detector distances, as described in Table S2. The value for Mn1.5-MO (0.036) is considered the maximum value for our experimental procedure.

distinguish the o-RS peaks from (222) and (400) of the spinel in well-crystalline samples.

e-LMNO (expanded LMNO). The third spinel phase is best identified in the low *Q*-region, as for Mn1.5-MO in Fig. 1a. A large strain makes it difficult to definitively identify the phase at high *Q*. A signature is lack of proper fitting of (220) in the XRD data, particularly a non-fitted intensity contribution for the low-angle part of (220). In some cases, this is first evident when visualizing the intensity data on a logarithmic scale (see Fig. 2).

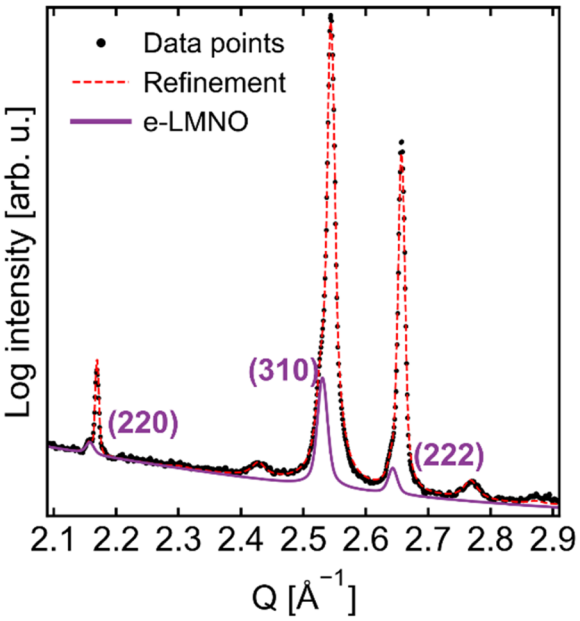

Fig. 2 Rietveld refined high-resolution SXRD data for Mn1.6-500C, highlighting the presence of e-LMNO with its relatively large intensity contribution at (220), and shoulders for (310) and (222).

This enhanced intensity is due to Mn/Ni in tetrahedral sites, and the peak shift is due to a change in the Li:Mn/Ni composition. When the mass fraction is significant a left shoulder is observed also on the main spinel peaks. Its lattice parameter varies a lot from sample to sample ($a \approx 8.21$–8.29 Å), but is generally less than the o-RS phase.[41] Another way to separate it from o-RS is that the (310) is more intense than (222), while it is opposite for o-RS. A relevant example is shown in Fig. 2. It is worth noting that throughout this work, as also the d-LMNO phase shows sign of Mn in tetrahedral sites, the e-LMNO phase is only included in the analysis if there are signs of two disordered LMNO-phases. That means if only one disordered LMNO phase is present, it will be denoted as d-LMNO.

N-layered RS. As the degree of distortion can vary, it is sometimes difficult to distinguish the hexagonal N-layered RS phase[56] from a cubic phase (this goes also for the M-layered phase, for which we refer to McCalla *et al.*[56] for more insight). This phase lacks intensity in the range of (220) discussed above. In general, this phase is identified by a low-angle shoulder to the spinel peaks, and notably on the high-angle side of o-RS-peaks. For instance, its most prominent peak, (104) at around 3.07 Å^{-1}, occurs in between the (400) peaks for the o-RS and spinel phases. Its presence is usually indicated in a refinement that fails to pick up all the intensity for low-angle shoulders of the spinel peaks. This is more pronounced at high *Q*. The high-resolution data in Fig. 3 show a shoulder that is not accounted for by an e-LMNO phase, or by an o-RS phase. We thus allocate these shoulders to the N-layered rock salt phase.

Samples with maximum order (MO)

The MO-samples were obtained upon slow stepwise cooling (see Experimental). Prior to cooling, their phase contents

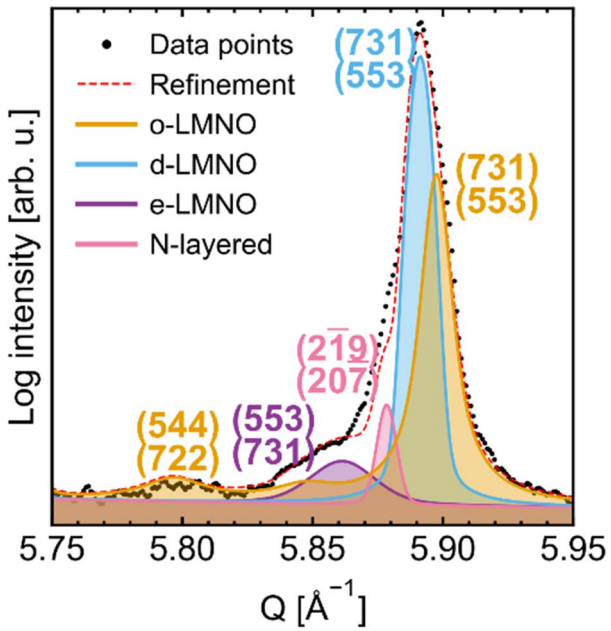

Fig. 3 Rietveld refined high-resolution SXRD data for Mn1.6-500C at high Q, showing all present phases – including the N-layered impurity. Miller indices are included. It is possible to distinguish these phases at high scattering angles, however, this is hardly possible at low angles (or for data with low resolution).

correspond to those of the quenched samples described below. We consider these MO-samples to be the most phase pure LMNO spinel materials that can be obtained within reasonable efforts.

The relative ordering (RO) was estimated for MO-samples of $LiMn_xNi_{2-x}O_4$, $x = 1.50, 1.55, 1.60, 1.70, 1.80$ and 1.90, based on eqn (3). The RO decreases rapidly with increasing Mn content, and for $x \geq 1.8$ no ordering can be detected, Fig. 1b. As mentioned, the RO-value cannot be translated into Mn/Ni site occupancies, since atomic displacements strongly contribute to the intensity of superstructure peaks owing to differences in Mn–O and Ni–O bond lengths. For ideal $Li_2Mn_3NiO_8$, one expects close to complete Mn and Ni ordering between 12d and 4a sites ($P4_332$). Based on previous neutron diffraction data, there are three Mn–O distances of around 1.91 Å, whereas the Ni–O bond is longer at 2.05 Å.[43] This implies that the (x, y, z) coordinates for the oxygen atom in the 24e site have major impact on the intensities of the superstructure reflections. Owing to the poor X-ray scattering contrast, we constrain the occupancies to 100% Mn in 12d and 100% Ni in 4a for all ordered phases and refine atomic coordinates while restraining the bond distances. The obtained bond lengths for Mn1.5-MO are 1.935(8) Å, 1.873(8) Å and 1.896(7) Å for the Mn–O bonds and 2.065(8) Å for the Ni–O bond. Similar values were obtained for Mn(1.55/1.6)-MO within estimated errors. Obtained atomic coordinates and bond lengths are given in Table S7.

The minority phases were included in the Rietveld refinements. Derived mass fractions and unit cell dimensions are compared for the spinel and rock salt type phases in Fig. 4a. Note that the x-axis represents the nominal sample stoichiometry, not the stoichiometry of the individual phases. Spinel phase(s) dominate for all MO-samples and except for Mn1.5-MO, significant amounts of d-LMNO are present. The real stoichiometries of the spinel phases can hardly be determined, however, the actual d-LMNO and e-LMNO stoichiometries are most likely shifted towards higher Mn contents relative to the sample average, whereas the stoichiometry of o-LMNO is close to $Li_2Mn_3NiO_8$.

The cubic a-axis is reported to vary linearly with the Mn content in LMNO.[39] The currently enhanced resolution in the PXRD data makes it possible to reveal peak splitting and finer details. To compare with previous data (see Fig. S6 for a comparison of various $LiMn_{1.5+x}Ni_{0.5-x}O_4$-sample series and reported lattice parameters[5,39,62–64]) a weighted average of the lattice parameters for all observed spinel phases is calculated, see Fig. 4b. It is not obvious that this relation is linear; (i) first, one would expect different impacts of Mn entering the 8c site (replacing Li(I)), the 4a site (replacing Ni(II)) and the 12d site; (ii) the effect of increased Mn content will be different for o-LMNO and d-LMNO and (iii) the presence of any amorphous/nanocrystalline impurity phases would affect the compositional analysis. Note that Mn1.5-MO is not following the trend (its lattice parameter is significantly larger than 8.163 Å as expected from linear extrapolation).

Just a minor rock salt impurity (0.2 wt%) is observed for the Mn1.5-MO sample. The o-RS phase is here refined in accordance with data on the $Ni_{6+2x}Mn_{1-x}O_8$-system[65] and the phase diagrams by McCalla *et al.*[41] From the expanded unit cell (a = 8.324(3) Å) we expect that the o-RS phase contain some Ni also in the 4a site. Although this impurity phase exists just in trace amounts there could in principle exist further (nano)domains (invisible to the diffraction) that hinder the refined o-LMNO phase to obtain its thermodynamically ideal Mn/Ni ratio of 3. The slightly enlarged lattice parameter for o-LMNO may reflect a redistribution (say 0.5 wt%) of transition metal onto tetrahedral Li sites as indicated by increased intensity of *e.g.* (422).[66] This has been reported for o-LMNO previously[67] and is supported by current findings, see Fig. S7, in terms of a small, yet significant, improvement of the fit, thanks to the extraordinary signal-to-noise ratio provided by the adopted Pilatus detector. Such redistribution is larger for d-LMNO, and even more prominent in e-LMNO, see below. This may explain why the current lattice parameters of the average spinel are slightly higher than reported by Zhong *et al.*,[39] nevertheless in line with Berg *et al.*[63] who adopted a similar synthesis approach with low temperature annealing (400 °C) that could promote formation of e-LMNO.[68]

The d-LMNO phase is well refined and contains a few percent Mn/Ni at tetrahedral sites based on the intensity gain of specific Bragg reflections. No clear conclusion can be drawn for the expanded spinel e-LMNO, in particular not for Mn(1.5,1.55,1.6)-MO due to the trace amounts. However, the lattice parameter for e-LMNO is rather well defined (Fig. 4a) and is larger than that of *e.g.* $LiMn_2O_4$ (8.24–8.25 Å).[39,63] Therefore the e-LMNO appears to be Li-deficient with some character similar to $[Li_{1-y}Mn_y]MnNiO_4$.[68] From interpolating the lattice parameters by Feltz *et al.* (Fig. S8) we estimate $y = 0.64$, 0.58 and 0.52 for

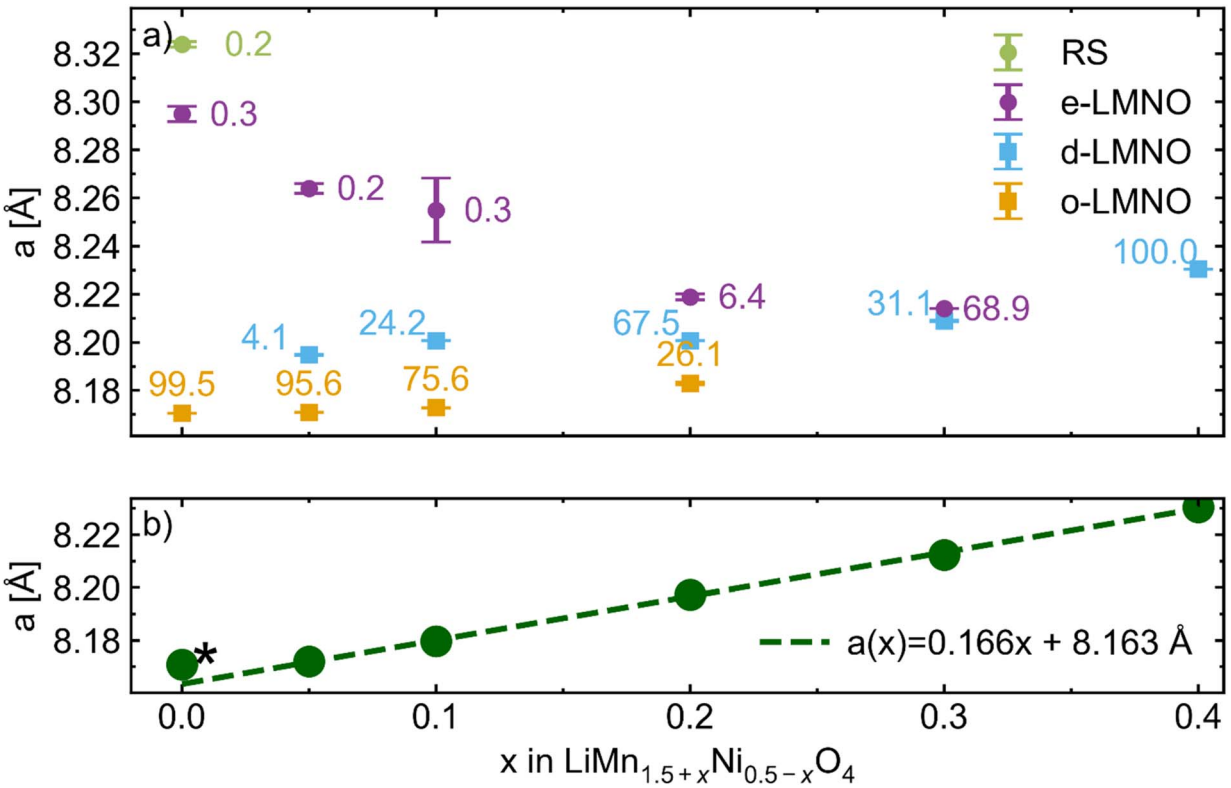

Fig. 4 (a) Phase content (weight percent written for each data point) and lattice parameters for LMNO-MO-samples with different stoichiometries. In Mn1.8-MO there are some very broad low intensity peaks, seemingly arising from a cubic structure with a lattice parameter of some 8.1 Å, which were included in a Le Bail peak fit. (b) The weighted average of the lattice parameters of the spinel phase(s) for each sample is plotted, and fitted to a linear function. For Mn-rich samples (*Mn1.5 is not included in the fit) a good linear correlation ($R^2 = 0.999$) is obtained, providing a useful relationship for estimating the Mn content of an LMNO spinel phase based on its lattice parameter.

Mn1.5-MO, Mn1.55-MO and Mn1.6-MO, respectively. For Mn1.7-MO the additional spinel phase has much lower lattice parameter and is well described as $LiMn_{1.8}Ni_{0.2}O_4$ without any clear evidence of Mn/Ni in tetrahedral sites. For simplicity, we still refer to this phase as e-LMNO. In general, whenever there is evidence of two disordered spinel phases, the one with the highest lattice parameter is labelled e-LMNO. Also, Mn1.8-MO shows two disordered LMNO phases, though with strongly overlapping peaks (see Fig. S9). On the other hand, Mn1.9-MO is dealt with as one phase. We emphasize that the results refer to samples subjected to the described heat treatment protocol and do not necessarily correspond to equilibrium for samples subjected to (multiply) repeated crushing, annealing and slow cooling.

As-synthesized materials quenched from 800 °C

The quenched (*Q*) samples represent materials that are commonly achieved after the initial synthesis, prior to subsequent treatments and annealing (see Experimental). By comparing the quenched and MO samples, we identify how annealing time, temperature and atmosphere affect the complex phase stability.

Disordered LMNO (d-LMNO) is the main component in all quenched samples. The *Q*-samples have two types of impurities. All samples contain a Ni-rich layered rock-salt related structure (N-layered). In Mn1.5-*Q* and Mn1.55-*Q* the second impurity phase is a rock salt phase (o-RS), whereas in Mn1.6-*Q* the second impurity complies with the Mn-rich layered phase (M-layered) as described by McCalla *et al.*[56] This suggests that the border between the three-phase regions SMN (spinel – M-layered – N-layered) and RSN (rock salt – spinel – N-layered) in the pseudo-ternary phase diagram at 800 °C, as described by McCalla *et al.*, is located between the Mn1.55 and Mn1.6 stoichiometries. The complex coexistence of phases is documented in the Rietveld refinements (Fig. S10), and the results are summarized in Table 1.

The N/M-layered phases are conveniently identified based on their lattice parameters. These were hence refined for samples located in the RSN- (Mn1.5-*Q* and Mn1.55-*Q*) and the SMN-regions (Mn1.6-*Q*). The chemical compositions were locked to $Li_{0.8}Mn_{0.34}Ni_{0.86}O_2$ and $Li_{1.22}Mn_{0.62}Ni_{0.16}O_2$ for the N- and M-layered phases, respectively, in line with previous reports. For both phases the Mn-atoms were fixed to the 3a site (the metal-layer), whereas for the N-layered phase the Li and Ni distribution on 3a- and 3b sites (the lithium-layer) was refined. Since compositions are uncertain, no bond length restraints were installed for these phases.

The diffraction peaks for the o-RS-phase with 32 available octahedral sites are reasonably well separated in the SRXD pattern. Hence, information could be extracted from Rietveld

Table 1 Refinement details for *Q*-samples. See Experimental for relevant crystallographic data. Calculated errors in parentheses. (*) Value was kept constant during refinement. (**) Estimated error is larger than the value itself. Mn1.6-*Q* contains in addition 2(1)% M-layered phase; a = 2.856(8), c = 14.30(5); fixed contents of 0.66 Li in 3a and 3.00 Li in 3b. Calculated average sample stoichiometry based on the refinements are given

	Sample	Mn1.5-*Q*	Mn1.55-*Q*	Mn1.6-*Q*
	$R_p/R_{wp}/R_{exp}$	4.2/5.9/2.5	3.3/5.0/2.4	2.0/3.2/2.6
d-LMNO	a (Å)	8.19303(9)	8.1902(1)	8.19381(6)
	wt%	89(1)	94(1)	94(2)
	TM in 8a	0.26(4)	0.22(4)	0.23(4)
	16d site	13.001(4) Mn	12.930(6) Mn	13.080(3) Mn
		2.999(4) Ni	3.070(6) Ni	2.920(3) Ni
N-layered	a (Å)	2.895(1)	2.895(5)	2.899(8)
	c (Å)	14.339(8)	14.33(3)	14.34(7)
	wt%	4.4(9)	3(1)	4(1)
	Li in 3a	0(**)	0(**)	0.009(**)
	Li in 3b	2.4(1)	2.4(3)	2.4(3)
o-RS	a (Å)	8.278(3)	8.282(5)	
	wt%	6.3(6)	2.5(7)	0.00(*)
	Li in 24d	6.00(*)	6.00(*)	
	Li in 4b	3.75(*)	3.75(*)	
Sample stoichiometry		$Li_{0.99}Mn_{1.51}Ni_{0.49}O_{3.84}$	$Li_{0.99}Mn_{1.56}Ni_{0.44}O_{3.9}$	$Li_{0.99}Mn_{1.6}Ni_{0.4}O_{3.92}$

refinements using a total of 43 peaks, of which 14 are well identified (note the log-scale in Fig. S11). For the isostructural Mg_6MnO_8 (ref. 69) and $Ni_{6+2x}Mn_{1-x}O_8$ (ref. 65) the otherwise empty 4b site is slightly filled by Ni upon Mn substitution. For the Li–Mn–Ni–O equilibrium phase, McCalla *et al.* claim that significant amounts of lithium occupy the 4b site. However, we cannot reliably determine the Li-occupation based on the powder XRD data. Hence, two assumptions are made; (i) full occupancy of Mn(IV) at the 4a site consistent with the parent structure Ni_6MnO_8 and (ii) every Li(I) substituting for Ni(II) in 24d is charge compensated, either by a neighbouring Mn(III) replacing another Ni(II) or by insertion of Li(I) into a 4b site. Using these charge neutrality assumptions, our findings are evaluated in view of the phase diagrams from Rowe[70] (quenching from 900 °C or 800 °C, in air) and McCalla *et al.*[41] (quenching from 800 °C in O_2). Results and details are given in Table S8 and Fig. S12. We note that significant differences in cation distribution result in only minor changes in R_{wp} and since these correlate strongly with O-coordinates, the distribution would be influenced by Mn/Ni–O bond length restraints. Our best composition estimate for o-RS in Mn1.5-*Q* and Mn1.55-*Q* is $Li_{0.307}Ni_{0.496}Mn_{0.197}O$ ($Mn[Ni_{3.94}Li_{1.50}Mn_{0.56}][Li_{0.94}O_8]$), which fulfills the charge neutrality criteria and is in line with previous work by McCalla *et al.*[41,56]

Due to the presence of Ni-rich impurities the actual Mn stoichiometry of the dominant d-LMNO phase will be higher than the average sample composition. The relative Mn/Ni occupation of the 16d site was settled based on unit cell parameters and the trend established by MO-samples (Fig. 4b). Based on the multi-phase Rietveld refinements, the average Mn content of the bulk sample was calculated and found to correspond well to the nominal composition, Table 1 (see also the section on validation of refinements).

One uncertainty worth mentioning is the possible presence of oxygen vacancies in the spinel structure.[41] However, our refinements cannot support any claim for O-vacancies in d-LMNO. Even though R_{wp} slightly improves, visual inspection (Fig. S13) reveals that the fit to some reflections like (222) is improved whereas it is worse for other reflections like (622).

Annealed samples: phase segregation, intermediate situations and realistic materials

The complexity and diversity evidenced by quenched and long-term annealed samples, reflect changes that occur within the processing window applied in both small and large scale LMNO synthesis. The essential phases are identified above in the studies of the *Q* and MO model samples. In this section we address time-dependent changes that occur for the *Q*-samples when annealed for 6 h between 400 and 750 °C in static air or in O_2-flow. An overview of changes is shown in Fig. 5 (O_2-treated samples) and S14 (air treated samples) in terms of annealing temperature and phases identified based on cubic (pseudo-cubic) unit cell dimensions.

Phase segregation induced by Mn/Ni ordering

The MO-samples show definite signs of Mn/Ni ordering, see above. For Mn1.55, Mn1.6, and Mn1.7 this implies either variations in the composition for the ordered $Li_2Mn_3NiO_8$ phase or a coexistence of ordered and disordered spinel with slightly different compositions. We observed evidence for the latter situation, whereas no such coexistence is indicated for any of the *Q*-samples. As seen in Fig. 6, the data for *Q*-samples after 6 h anneal prove a progressing phase segregation, most pronounced in Mn-rich samples. At the onset of ordering and under conditions where lattice parameters are almost equal for o-LMNO and d-LMNO, this segregation can hardly be followed by diffraction, and in any case high-resolution data are required (see Fig. S16). Whenever we observe an asymmetrical peak shape, it is reasonable to claim the coexistence of two spinel phases, where the smaller volume variant represents o-LMNO.

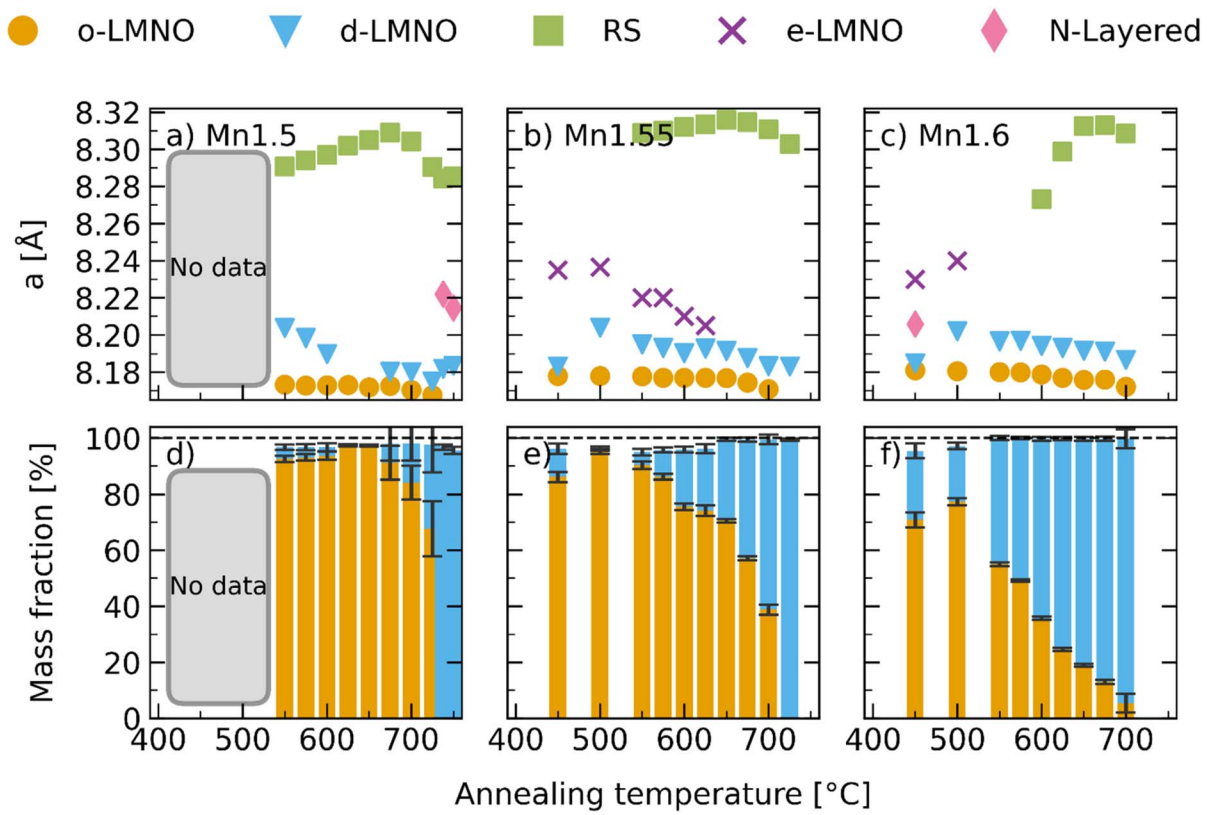

Fig. 5 Cubic (or pseudo-cubic for the N-layered phase) unit cell dimensions of samples annealed in O_2-flow at temperatures between 400 and 750 °C, for (a) Mn1.5-, (b) Mn1.55- and (c) Mn1.6-samples. The corresponding mass fractions of the two main spinel phases, d-LMNO and o-LMNO are respectively in (d)–(f). Here, the small deviation from 100% reflects impurities, typically <5 wt%, see below.

The detection of coexisting spinel phases is hampered by their similarity in lattice parameter and by peak overlap from impurity phases. It may easily escape detection in the home-laboratory, in particular for low Mn content, low annealing temperatures, and annealing in air. Currently, the unique superstructure peaks of o-LMNO in the synchrotron data allows precise determination of lattice parameters. By implementing the procedures and phases as described in the Experimental section, mass fractions of o-LMNO and d-LMNO were determined, see Fig. 5d–f (annealing in O_2) and S14d–f (annealing in air). The trend of increasing the mass fraction of d-LMNO at higher annealing temperatures correlates with decreasing lattice parameters for both o-LMNO and d-LMNO. Both phases are thus becoming less Mn-rich upon higher temperature

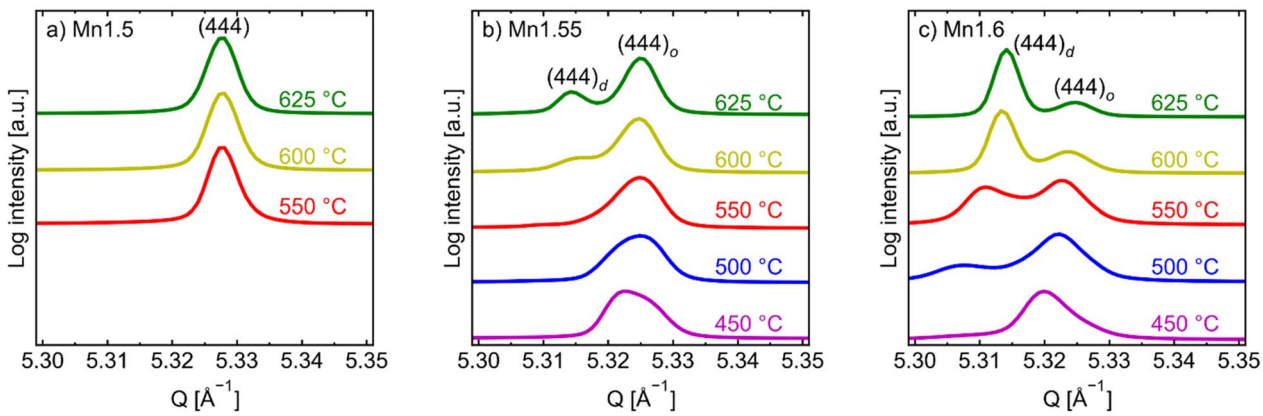

Fig. 6 SXRD-data (optimized detector position) for samples annealed 6 h in O_2-flow at different temperatures. From top to bottom; 625 °C (green), 600 °C (yellow), 550 °C (red), 500 °C (blue) and 450 °C (purple). Peak splitting is clearly visible in the Mn-rich samples, with subscripts o (for o-LMNO) and d (for d-LMNO). A corresponding plot is given in Fig. S16 for a different detector position, highlighting challenges with inferior instrumental resolution.

annealing. The weighted average lattice parameter of these two phases (interpreted as the average LMNO composition in the sample) however stays rather constant throughout the heating series as the relative mass fractions change. This is highlighted in Fig. S14 (air) and S15 (O_2), where the weighted lattice parameter average for the spinel phases is plotted for all samples.

The peak splitting – which is a definite token of Mn/Ni ordering (and thus o-LMNO/d-LMNO coexistence) – sets in at very low temperatures, already seen from annealing Mn1.6 at 400 °C (see Fig. S14). As the ordering process strives towards a 3-to-1 ratio of Mn and Ni, possibly for charge balance and/or strain reasons, ordered islands are formed and the disordered spinel phase becomes enriched in Mn. The difference in composition between o-LMNO and d-LMNO is thus enhanced by the Mn/Ni ordering. The strain decreases with higher annealing temperatures for o-LMNO (Fig. S17a and b), whereas it increases for d-LMNO when more o-LMNO is present (Fig. S17c and d).

As seen also in the MO-samples, we note that d-LMNO always has a certain occupancy of Mn/Ni atoms on tetrahedral 8a sites. This correlates with increased lattice parameter for d-LMNO, which again results in a more pronounced peak splitting between o- and d-LMNO. This Mn/Ni redistribution is dynamic with maximum impact for the 8a sites at 650 °C for Mn1.55 (5% Mn in 8a) and at 550 °C for Mn1.6 (2% Mn), after annealing in O_2-flow, Fig. S17e and f.

We emphasize that the precipitated Ni-rich impurities have a significant effect on the unit cell dimensions of the spinel majority phase. This effect is probably overlooked in many studies. The o-RS is thus of practical relevance, both for the ordering process and for locking up nickel in an inactive electrochemical state.

Impurity phases: the rock salt phase (o-RS)

A small amount of rock salt impurity is frequently present in LMNO but is challenging to fully characterize. In all quenched samples the o-RS impurity is quite prominent, but upon annealing the impurity phase disappear gradually. The o-RS impurities are of $MnNi_6O_8$-type[41] with lattice parameters significantly smaller (~8.28–8.32 Å) than those of NiO (8.36 Å for the $MnNi_6O_8$-type supercell[71]).

The incorporation of Li into the o-RS phase leads to shorter lattice parameters. As already introduced above, two substitution routes appear feasible: mechanism 1 where every Li(I) substituting for Ni(II) at the 24d site is charge compensated by an additional Li(I) in an empty 4b site; and mechanism 2 where charge compensation occurs by replacing a second Ni(II) by Mn(III). According to unpublished DFT-work,[72] mechanism 1 would result in a (linear) lattice parameter change on Li-substitution, whereas no such change is seen for mechanism 2.

Fig. 7 shows the variation of lattice parameters and mass fractions of the o-RS phase in Mn1.5 and Mn1.55 for different annealing conditions. The *a*-axis varies significantly, demonstrating that temperature-driven compositional changes occur. The refinements indicate correlations between the *a*-axis and

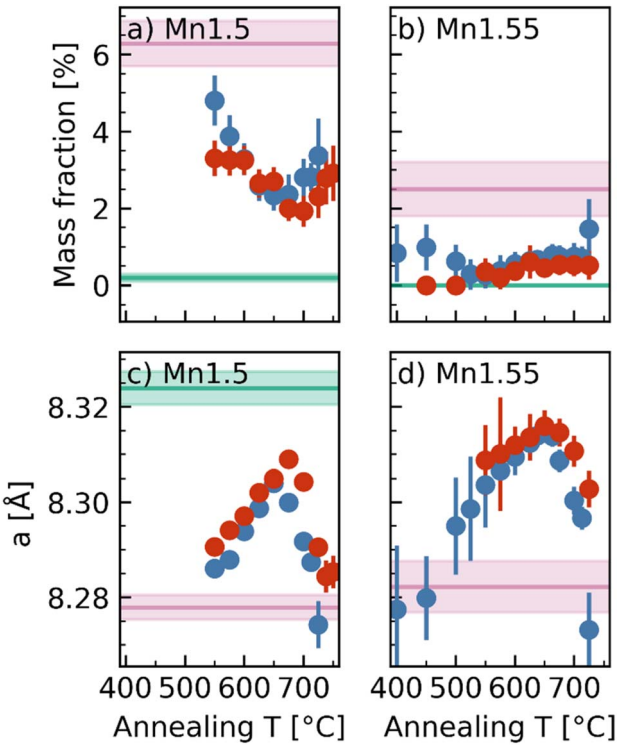

Fig. 7 (a and b) o-RS mass fractions and (c and d) lattice parameters from Rietveld refinement of samples annealed 6 h at different temperatures, in O_2-flow (red) or in air (blue). Lines show corresponding values for quenched (*Q*, purple) and maximum ordered (MO, green) samples.

the refined Li-content in the 24d site (Fig. S18) as well as bond-distances (Fig. S19). The clear, yet moderate variations in the lattice parameter (8.28–8.32 Å) seen in Fig. S20 can be accounted for by realistic variations in the Li-content (z), using the relation given in eqn (4), with 8.32 Å as the reference value for the parent compound, $MnNi_6O_8$ (ref. 65 and 73) and a_{RS} the lattice parameter of the o-RS phase.

$$z = \frac{\left(8.32\ \text{Å}\right)^3 - {a_{RS}}^3}{\left(8.32\ \text{Å}\right)^3 \times 0.0163} \quad (4)$$

Hence, we conclude that mechanism 1 is operative for $[Mn]_{4a}[Ni_{6-z}Li_z]_{24d}[Li_z]_{4b}O_8$. This is a reasonable simplification, as published phase diagrams[41] suggest that samples (after "regular cooling" from 800 °C) contain an o-RS phase with ~15% Mn, in fair agreement with the current values of 14% for $x = 0$ and 12% for $x = 1$. Further details including bond distance restraints, along with simulated diffraction patterns for different site-filling schemes are provided in the SI, *e.g.* Fig. S2.

For samples annealed in air, the *a*-axis of the o-RS impurity obtains a maximum after annealing ~650 °C, Fig. 7a and b. In general, the *a*-axis of the o-RS phase after 6 h annealing at a specific temperature is largest for Mn-rich bulk samples. We believe that the actual Mn-amount remains quite unchanged, hence, the increase in the *a*-axis is rather attributed to a more

effective Li-removal from o-RS upon annealing – and possibly indicating that equilibrium is not reached after 6 h. This assumption was strengthened in an *in situ* study of annealing Mn1.5-*Q* at 650 °C (Fig. 8). Here we observed a continuous change in the lattice parameter for the o-RS phase, which shows that the equilibrium composition is not reached within a time-frame of 15 h.

The o-RS weight fraction varies with nominal Mn content and thermal history (Fig. 7c and d). Both Mn1.5 and Mn1.55 contain less o-RS after annealing, as seen from comparing with the purple line representing the quenched starting-material (*Q*). Hence, the initial o-RS precipitation at 800 °C is partly reversed on subsequent annealing. The data show that the oxygen holding atmosphere destabilizes o-RS and reforms LMNO spinel. This is evident from the data on Mn1.55-samples at $T <$ 550 °C where O_2-flow removes all the o-RS. For Mn1.5, a higher annealing temperature is required for reducing the o-RS amount; with minimum amounts of o-RS achieved at 700 °C in O_2-flow and 650 °C in air. Mn1.6 behaves differently, Fig. S22. Here, no o-RS is present in the starting material (Mn1.6-*Q*). Nevertheless, tiny amounts of o-RS forms at $T >$ 525 °C in air and $T >$ 600 °C in O_2. The diffraction peak profiles give some information on crystallite size and strain, however, these parameters are strongly correlated and the uncertainty is considerable (Fig. S22). It appears that the o-RS crystallite size increases during annealing, from around 30 nm in Mn1.5-*Q* to around 50–150 nm, and that strain is decreasing as lattice parameter increase. This suggests fewer, but larger, o-RS crystallites after annealing.

Impurity phases: the third spinel phase (e-LMNO)

After annealing at moderate temperatures (<625 °C) the samples exhibit shoulders on the low-angle side of the spinel peaks along with certain intensity changes. These features are not observed for the quenched (*Q*) samples and are weakly developed in the MO samples (<0.5 wt%). This is considered as a signature of an expanded spinel phase (e-LMNO) that represents an intermediate stage in the restructuring process of *Q*-samples upon annealing. Above some 600 °C these shoulders/peak broadening are hardly distinguishable.

The refined lattice parameter for e-LMNO – along with mass fraction and amount of Mn at tetrahedral sites – are shown for Mn1.55 in Fig. 9, and for Mn1.6 in Fig. S23. For Mn1.5, we only observe one disordered spinel phase and thus attribute the phase to d-LMNO, as discussed in the section on identification of impurity phases. The e-LMNO has rather high lattice parameter after 6 h annealing, largest after low annealing temperatures and for MO-samples (green line in Fig. 9). This temperature variation indicates that the Li/Mn/Ni redistribution is dynamic and that long annealing times are required to reach a "final" state. The involved structural changes extend beyond the formation of Mn-enriched octahedral sites (approaching that of $LiMn_2O_4$ with $a = 8.243$ Å),[39] since the intensities for *e.g.* (220) clearly indicate that the tetrahedral sites must contain significant amounts of Mn/Ni, relative to the situation for d-LMNO. In Fig. 9c it is worth noticing that the amount of Mn in the 8a-site is increasing for lower annealing temperatures, except for the lowest annealing temperature, 400 °C in air. The diffraction peaks of e-LMNO are very broad at high scattering angles, due to high strain in addition to rather small crystallites (<100 nm, but hard to determine accurately), and are hence difficult to separate from background. The strain is considerable after low temperature annealing, Fig. S24.

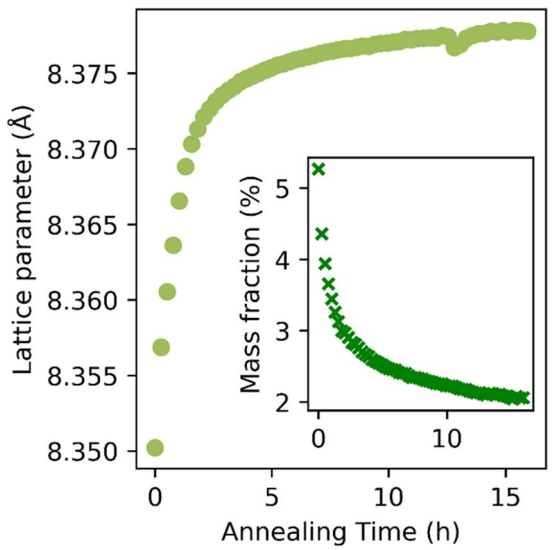

Fig. 8 o-RS details plotted from *in situ* SXRD of Mn1.5-*Q* annealed in air at 650 °C, showing the time dependant changes of the lattice parameter and the mass fraction (inset).

Impurity phases: the N-layered phase

The N-layered hexagonal phase can be described within a (pseudo)cubic unit cell $a_{cubic} = b_{cubic} = a_{hex} \times \sqrt{8}$ and $c_{cubic} = c_{hex}/\sqrt{3}$. McCalla *et al.* suggested that the N-layered structure represents an equilibrium phase at 800 °C. We observe this phase for Mn1.6 samples annealed at 450–500 °C and for Mn1.5 samples annealed at $T >$ 725 °C, with a mass fraction of 1–3%, see Fig. S25. Even in the quenched samples with a significant content of the layered phase, its composition can hardly be determined from Rietveld refinements due to low intensities and severe peak overlap. This is especially the case for Mn1.6-samples, see the huge uncertainty as represented by the red areas in Fig. S25. Worth noting is the increased amount of the N-layered phase for the annealed Mn1.6-samples, and that the lattice parameters differ significantly from those of Mn1.6-*Q*. The *a*-axis remains quite constant (2.88–2.90 Å) whereas the *c*-axis changes from ~14.2 to ~14.4 Å. Pseudo-cubic lattice parameters are shown in Fig. 5 (annealed in O_2-flow) and Fig. S14 (annealed in air), hexagonal *a*- and *c*-lattice parameters are shown in Fig. S25. Note that the N-layered phase is readily removed by an annealing step within the range 525–700 °C.

Validation of methodology

To validate the quantitative Rietveld XRD analysis, the refined composition and mass fraction of each phase were used to backtrack the overall stoichiometry of each bulk sample, *i.e.*

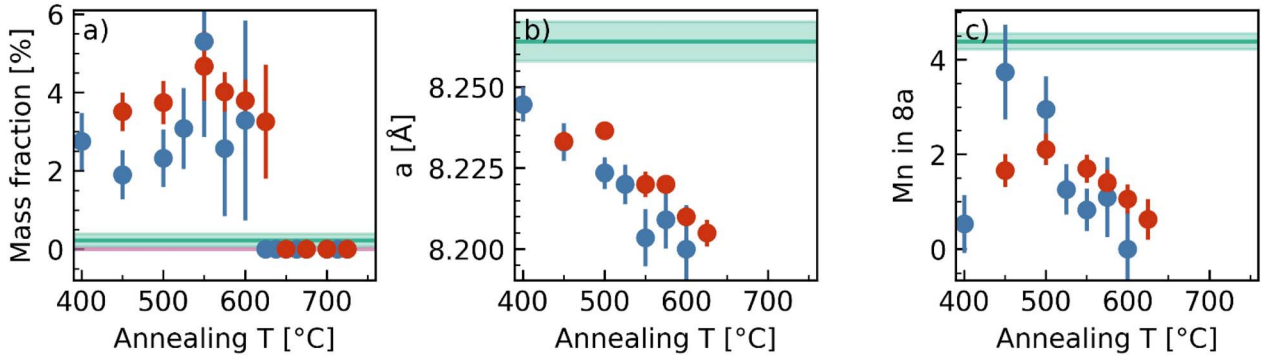

Fig. 9 Details on e-LMNO, the cubic high-Mn-spinel impurity, for the Mn1.55-series. The (a) mass fraction, (b) lattice parameter and (c) the refined amount of Mn-ions at the Li site, 8a, in samples annealed at different temperatures in O_2-flow (red) or in air (blue), relative to the values for the maximum ordered sample (Mn1.55-MO, green line). The quenched starting material (*Q*, purple line) has zero content of e-LMNO.

Mn1.5, Mn1.55 and Mn1.6. In these endeavours, the composition of o-LMNO is set as stoichiometric $Li_2Mn_3NiO_8$. The Mn content of d-LMNO/e-LMNO ($[Li_{1-y}Mn_y]Mn_{1.5+x}Ni_{0.5-x}O_4$) is based on (i) the trend shown in Fig. 4b for lattice expansion due to excess Mn in 16d site ($\Delta a_{16d} = 0.166$ Å $\times\, x$), and (ii) the lattice expansion due to Mn on tetrahedral 8a sites, applying the variation of lattice parameters for $[Li_{1-y}Mn_y]MnNiO_4$ according to Feltz *et al.*[68] ($\Delta a_{8a} = 0.289$ Å $\times\, y$). Assuming that this also applies to $[Li_{1-y}Mn_y]Mn_{1.5+x}Ni_{0.5-x}O_4$ then less Mn is required into the 16d site to achieve the same expansion (since substituting Mn for Li at the 8a site leads to an expansion ~1.74 times larger than that achieved by substituting for Ni at the 16d site). The excess Mn, x, can thus be estimated from the refined datasets (eqn (5)) based on the extrapolated lattice parameter for stoichiometric LMNO (8.163 Å, as seen in Fig. 4b).

$$x = \frac{a - 8.163\ \text{Å}}{0.166} - 1.74y \qquad (5)$$

The overall Mn/Ni ratios in each sample were calculated based on the Rietveld refinements and are plotted in Fig. 10. The currently reported Li-contents (Fig. S26) were normalized relative to the total amounts of Mn and Ni and are in excellent agreement with the ICP-OES data (*e.g.* a reported Li-content of 1.00 means there is twice as much Mn + Ni than Li, in line with what is expected for LMNO). We note some discrepancy in the calculated compositions, ascribed to low Li-scattering power and poor Mn/Ni scattering contrast. Nevertheless, the *Q*-samples (purple lines) comply well with the expected Mn/Ni contents of 3, 3.44 and 4 (dashed black lines) for Mn1.5-*Q*, Mn1.55-*Q* and Mn1.6-*Q*, respectively. However, for the most ordered samples (except Mn1.5-MO) the Mn content is underestimated. There are several possible sources for this inconsistency; (i) the o-LMNO phase can be Mn-enriched, (ii) the o-RS-phase composition could be adjusted according to eqn (4), (iii) some Mn can be located in antiphase boundaries and escape detection, and not least, (iv) discrepancy in the assumed composition of the layered phase. In conclusion, the applied approach is highly appropriate; however, more detailed information on phase compositions is needed, *e.g.* as provided by combined X-ray and neutron diffraction experiments.

Mn/Ni ordering and RO

As described in the Experimental section, it is hardly possible to determine the Mn/Ni distribution with respect to the 12d and 4a sites (space group $P4_332$) by means of XRD. The main reason is that the intensity of the superstructure reflections is dominated by shifts in the (oxygen) atomic coordinates. This will not be a major issue in the case of powder neutron diffraction data.

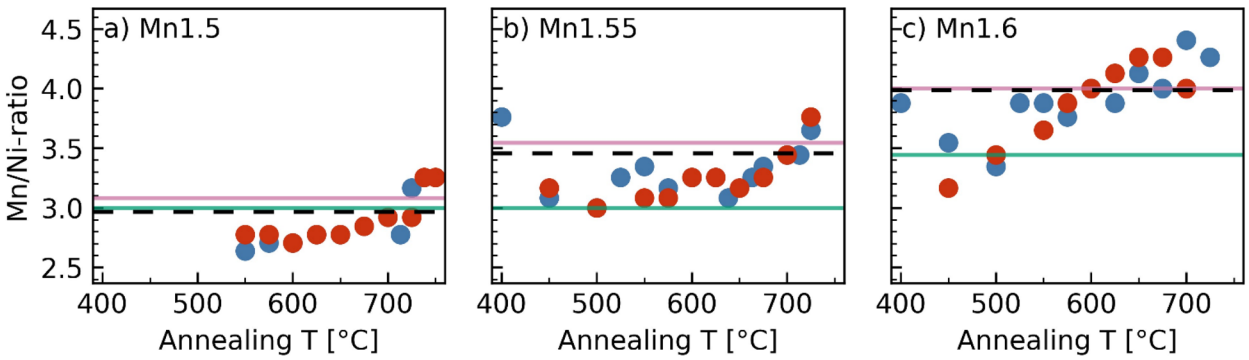

Fig. 10 Estimated sample stoichiometries based on Rietveld refinement of annealed samples of (a) Mn1.5, (b) Mn1.55 and (c) Mn1.6. Corresponding values for quenched (*Q*, purple lines) and maximum ordered (MO, green lines) samples are included. Values based on ICP-OES are shown by dashed black lines.

Furthermore, Raman spectroscopy is sensitive to the local symmetry and the o-LMNO and d-LMNO are easily distinguished in terms of observed vibration modes. Below we compare XRD and Raman spectroscopy results.

The synchrotron diffraction data allows us to quantify the growth (integrated intensity) and size of ordered domains (peak width), unit cell dimensions and phase fractions (Rietveld analysis) as function of annealing conditions. Fig. 11a–c shows derived RO-values for *Q*-samples subjected to 6 h annealing. The pO_2 has a pronounced effect, in particular for Mn1.5, which is disordered at 725 °C when annealed in air, but ordered in O_2-flow, which is in line with literature.[8] The underlying mechanism is not clearly established. We observe that a lower pO_2 tends to stabilize o-RS or N-layer impurities that have a lower average oxidation number for the transition metal cations compared to LMNO, and these are Ni-enriched. A higher pO_2 stabilizes Mn(IV) and lower the amount of manganese in tetrahedral sites, which in turn stabilizes the spinel phase. Since the o-RS and N-layer precipitation reactions involve formation of new phases, these do not need to generate O-vacancies in the spinel phase itself. To our knowledge, there are currently no neutron diffraction data addressing the complexity of the segregation of these impurity phases and the induced changes in the spinel structure.

It is noteworthy that the ordering process for Mn1.55 and Mn1.6 sets in at a lower temperature compared to Mn1.5, even though the latter has the optimum composition for complete Mn/Ni order. The fact that ordering is achieved already at 400–450 °C implies that cation diffusion is rapid already at such low temperatures, which we attribute to the numerous available cation sites in the ccp anion lattice of the spinel. To our attention, such low ordering temperatures has not been reported previously, except for delithiated samples.[74] This shows that the properties of a batch of LMNO depend not only on synthesis route, cooling procedure, atmosphere, and typical medium temperature annealing temperatures, but also on the cooling speed and time. For Mn1.55 and Mn1.6, the RO is gradually reduced at higher annealing temperatures, whereas for Mn1.5 the RO remains high up to a maximum temperature of 725 °C in O_2-flow for the current study (713 °C in air).

The size of the ordered domains (D_O) is estimated from the FWHM of the superstructure peaks using the Scherrer equation as explained in the Experimental section (eqn (1) and (2)). The domain size is somewhat smaller for Mn1.5-MO (~100 nm) than for Mn1.55-MO and Mn1.6-MO (~130 nm), Fig. 11d–f. The domain sizes for the MO samples represent the final stage of the growth process. These domains ultimately fill the entire crystallite volume and are separated by (anti-phase) boundaries at the atomic level. Domain nucleation in the quenched samples begins at relatively low temperatures. After 6 h annealing at various temperatures, Fig. 11d–f, the domains have not yet reached the size as seen for MO-samples. For 6 h anneal, the domains in Mn1.6 reach their largest size at some 500 °C, where also the RO is highest. There are correlations between domain size and RO; however, other factors also play a role. This is evidenced by Mn1.55 where the largest domains occur at 700 °C,

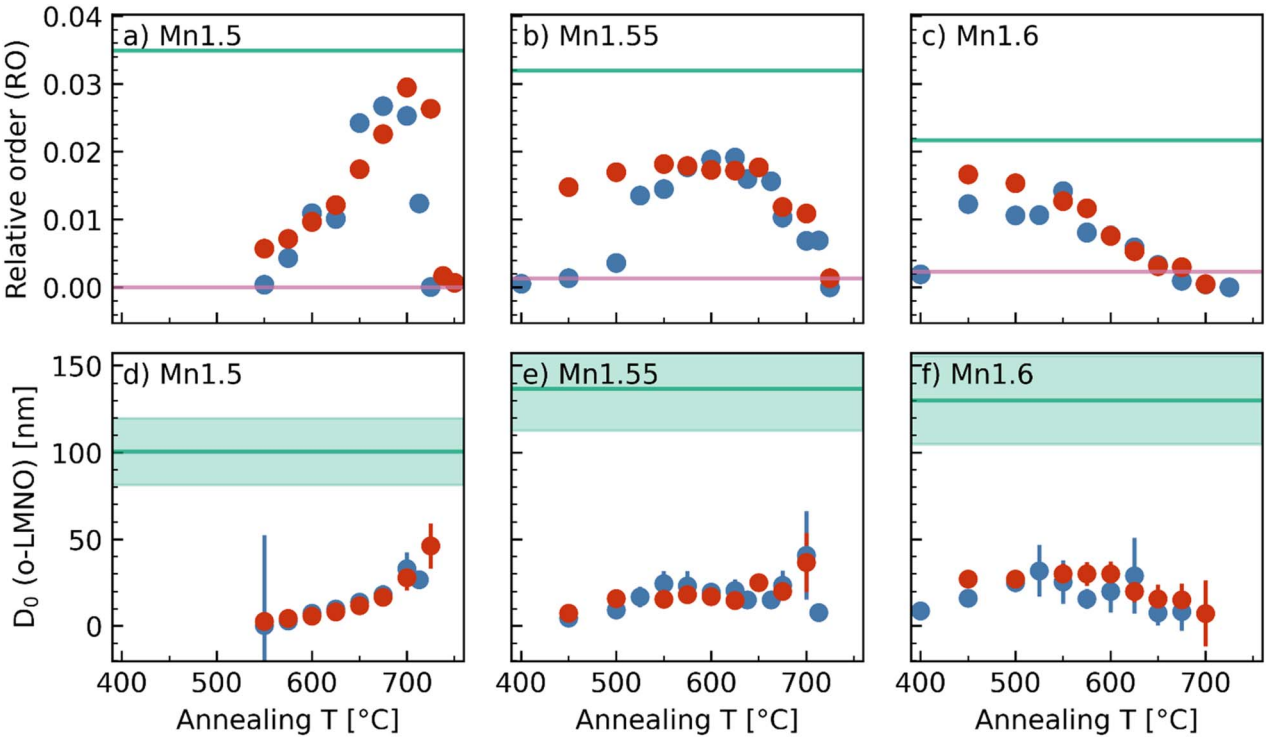

Fig. 11 (a–c) Relative order (RO) calculated according to eqn (3) for samples annealed in air (blue) or O_2-flow (red), relative to the situation for the quenched starting material (*Q*, purple line) and the maximum ordered sample (MO, green line). (d–f) Size of the ordered domains, based on evaluation of superstructure peaks of o-LMNO found from Rietveld refinement and the Scherrer equation, eqn (1), and (2).

yet the RO is low, approximately 0.01. At higher annealing temperatures RO is decreasing without necessarily leading to smaller ordered domains. This is evident in the Mn-rich samples, but also for Mn1.5-713C. This suggests that above a certain temperature (depending on stoichiometry), ordering may still occur, but it may be limited to a few domains.

Ordering as seen by Raman spectroscopy

Whereas the diffraction analysis requires a minimum domain size of ~5 nm, Raman spectroscopy is sensitive to local symmetry and complements diffraction by enabling the detection of even smaller ordering domains. Fig. 12 compares Raman spectra for the *Q*- and MO-samples. The cation ordered state is manifested by a large number of additional modes. Based on the number and intensity of modes, the current Mn1.5-MO and Mn1.55-MO samples appear to be among the most ordered LMNO materials reported to date.[64]

The spectra obtained during scanning of different parts of the anticipated homogeneous samples were not fully reproduced. Raman exhibits a relatively low penetration depth, likely below 160 nm in our case (160 nm was assumed by Boulet-Roblin[44] *et al.* using a longer wavelength than used in our work). As a result, Raman probes a much smaller sample volume than XRD. A relevant example of an ordered bulk material with characteristics of a disordered surface region is presented in Fig. S27, highlighted by two sets of data points for some of the samples in Fig. 13. As a measure of the degree of ordering, the intensity ratio of the peaks around 162 and 496 cm^{-1} is utilized. The 496 cm^{-1} peak is not very sensitive to the degree of ordering, whereas the peak at 162 cm^{-1} is a T_{2g} mode connected with Li sublattice vibration[75] and is highly sensitive to the Mn/Ni ordering in the spinel. The latter is furthermore not significantly affected by neighbouring signals. In some studies the 638 cm^{-1}-peak is used instead,[76] and the resulting ratios of 638 cm^{-1} and 496 cm^{-1} are seen in Fig. S28. However, the 638 cm^{-1}-peak is highly influenced by Ni-rich impurity phases (typically 600–650 cm^{-1}) and is related to the Li–O1-distance[44] in o-LMNO – which is influenced by Mn, but less by Ni (as this does not bond to O1).

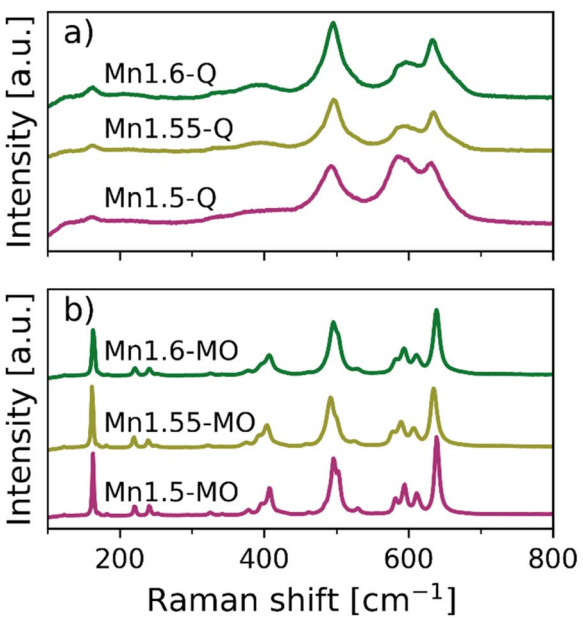

Fig. 12 Raman spectra of (a) *Q*-samples heated at 800 °C before quenched (disordered) and (b) MO-samples cooled very slow in O_2-flow (ordered). The peaks around 160 cm^{-1} and 500 cm^{-1} are used as means to compare the degree of ordering.

An unavoidable complexity arises for the 500 cm^{-1} region, affecting the use of the 496 cm^{-1} peak intensity. As shown by Dokko *et al.* the intensity decreases for more Mn-rich samples, which has been attributed to Ni(II)–O stretching.[77] This region can be influenced by impurities, *i.e.* an NiO-like RS impurity displays peaks from phonon scattering around 500 cm^{-1} (ref. 78) and the layered impurity phase contributes within the range 400–700 cm^{-1}.[79] Therefore, this approach is useful for comparing samples with similar stoichiometries but should not be used to quantify Mn or Ni at their respective sites.

High intensity ratios for the 162 *versus* 496 cm^{-1} peaks observed for Mn1.5-MO and MO1.55-MO point towards a high degree of ordering. Interestingly, according to the Raman data, the Mn1.5-sample annealed at 700 °C in air is more ordered than Mn1.5-MO, see Fig. 13. This probably reflects the length scale for the order and fluctuations due to beam and focus point (*e.g.* more/less impurity phases in the illuminated part of the sample). Similarly, several Mn-rich samples show both ordered and disordered characteristics, depending on the focus point (see the two data points for Mn1.55-625C and Mn1.6-625C in Fig. 13), probably reflecting the physical coexistence of ordered and disordered spinel phases. Significant ordering is furthermore detected already at 525 °C for Mn1.5, *i.e.* at lower temperatures than detected by SXRD for this stoichiometry (where 575 °C was the lowest temperature with detectable superstructure peaks). Raman data further support the SXRD refinements by showing that Mn1.6-400C and Mn1.55-450C do indeed exhibit cation ordering. In these samples the splitting of the main spinel peak(s) was the only indication of ordering in the SXRD data, as the superstructure peaks were not visible (RO = 0 as seen in Fig. 11b and c). Interestingly Mn1.55-400C is the only low temperature Mn-rich sample that shows no signs of ordering. This, together with the strong indications of no tetrahedral Mn in the sample (Fig. 9c) clearly suggests a link between o-LMNO and e-LMNO at low temperatures.

This study aligns with the recent research conducted by Stüble *et al.*[64] We note that all Raman modes reported in their work are also present in the Mn1.5-MO, Mn1.55-MO and Mn1.6-MO samples (even for Mn1.7-MO many of the modes are observed). In addition to these, we observe additional modes, which are predicted based on DFT-calculations by Miwa,[80] and listed in Table S9.

Electrochemical characterization and *operando* SXRD

A brief assessment of the electrochemical behavior is given for samples prepared according to Table S10. These data give an estimate of the ratio of electrochemically active Ni and Mn in the samples, and therefore also the relative amount of inactive

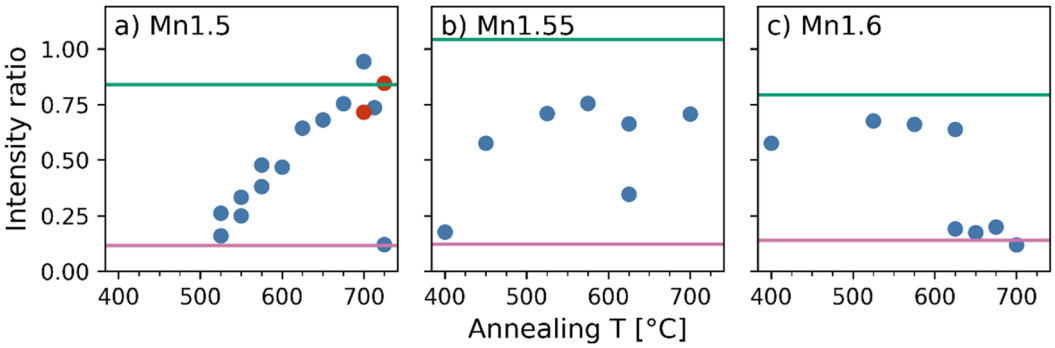

Fig. 13 Using Raman spectroscopy to quantify of the degree of Mn/Ni ordering based on relative intensity maxima (ratio between Raman modes at 162 and 496 cm^{-1}) as function of annealing temperature for (a) Mn1.5, (b) Mn1.55 and (c) Mn1.6-samples heated in air (blue) or O_2-flow (red). Comparison with the quenched starting material (*Q*, purple line) and the maximum ordered sample (MO, green line). For *e.g.* Mn1.55-625C and Mn1.6-625C more spots were measured to illustrate material variations.

Mn(IV) and active Mn(III). As shown in Fig. S29 all Mn-rich samples have close to the expected ratio of capacity coming from Mn-activity. That is 26(3), 44.4(5), 60(2) and 78(1)% of the capacity comes from below 4.4 V *vs.* Li/Li^+ for Mn1.6, Mn1.7, Mn1.8 and Mn1.9, respectively. For Mn1.5 the percentage is higher than expected, 8.6(5)%, mainly as a consequence of the presence of o-RS. These experiments provide an indirect estimate of the amount of o-RS, *i.e.* the amount of Ni being less capable of participating in the (de)lithiation process due to trapping. Such trapping is almost non-existing in Mn-rich samples, as documented by the very weak o-RS peaks in the diffractograms, see Fig. S30.

These data fail however to describe effects connected to the ordering of the spinel. Even though o-LMNO and d-LMNO have different electrochemical characteristics for their Ni-plateau (different voltages for $Ni^{2+/3+}$ and $Ni^{3+/4+}$, with a separation that decreases from ~70 to ~20 mV as LMNO orders[6,8,13,19,81]), these cannot be discriminated when the sample contains both o-LMNO and d-LMNO in addition to other electroactive phases (N/M-layered impurities are electroactive; the contribution from o-RS is almost negligible[82]). The e-LMNO phase is invisible due to its tiny molar fraction and its electrochemical properties remains unknown.

To better understand the effect of the different phases on the electrochemical performance, a model material (Mn1.6-500C-72 h) was synthesized and subjected to 72 hours of annealing in O_2-flow (for details see Table S11). We emphasize that a proper electrochemical assessment of the long-term stability of the different phases within the cathode material, require full cell studies,[83] *i.e.* an optimized high-voltage compatible electrolyte and a relevant anode material must be in place. Currently, we report on half-cell studies (Li metal as anode), in line with most works in literature. We focus on an expanded voltage window down to 1.5 V which enable us to distinguish electrochemical effects for the different phases as excess Li is being inserted into empty (interstitial) sites. In this way we exploit the "unlimited" Li-reservoir in the anode, and explore the reversibility upon pushing excess Li into materials with different degrees of cation ordering.[17,84] This cycling program also accelerates the degradation process. For Mn1.6-500C-72 h, Fig. 14a shows that the discharge capacity has degraded to 70% of the initial value already after 50 cycles (comparable to the report of Lee *et al.* for cycling down to 2.0 V[17]). By comparing the capacity contributions from the different voltage ranges, shown in Fig. 14b, the electrochemical performance can be correlated with crystal structure information – especially in combination with *operando* SXRD data. From the pure electrochemical assessment in Fig. 14b we conclude that the main drivers for reduced capacity are decreasing $Ni^{2+/3+/4+}$ activity (>4.4 V) in addition to the loss of Mn-activity at the lowest potentials (<2.1 V).

In Mn1.6-500C-72 h the difference in lattice parameters between o-LMNO and d-LMNO is sufficiently large to be identified by the Dexela-detector of BM31 (SNBL, ESRF), see Fig. S31, even in a situation with interference from a number of components in the *operando*-cell (custom cells based on the design by Drozhzhin *et al.*[85]). However, peaks arising from o-RS can barely be observed in this setup (see Fig. S32), probably due to the low quantity and the limited signal-to-noise ratio in *operando* data. This highlights that systematic post mortem studies are required to explore any change in the impurity phases during cycling. Fig. S33 shows the electrochemical cycling data alongside diffractograms for two charge/discharge cycles (1.5–5 V) for Mn1.6-500C-72 h, highlighting prominent phase changes. The diffraction data in Fig. 14c is showcasing the low voltage behaviour, with two Li-rich tetragonal phases emerging (T1 and T2). A Rietveld refinement was performed for the low-voltage region (for details, see the figure caption of Fig. S33) and the derived relative mass fractions as a function of discharge voltage are shown in Fig. 14d. Interestingly, o-LMNO transforms first (seemingly into the tetragonal variant T1), whereas d-LMNO does not degrade noteworthy until it reaches down to 2 V, whereafter the growth of T2 increase significantly. This is interesting, as d-LMNO is reported to accept excess Li at a higher voltage (discharge plateau starting already at 2.3 V according to Lee *et al.*[17]). This may be due to the Mn-rich composition of d-LMNO in the current Mn1.6-500C-72 h sample. The semi-simultaneously measured XANES data (Fig. S33) show that the oxidation state and local environment

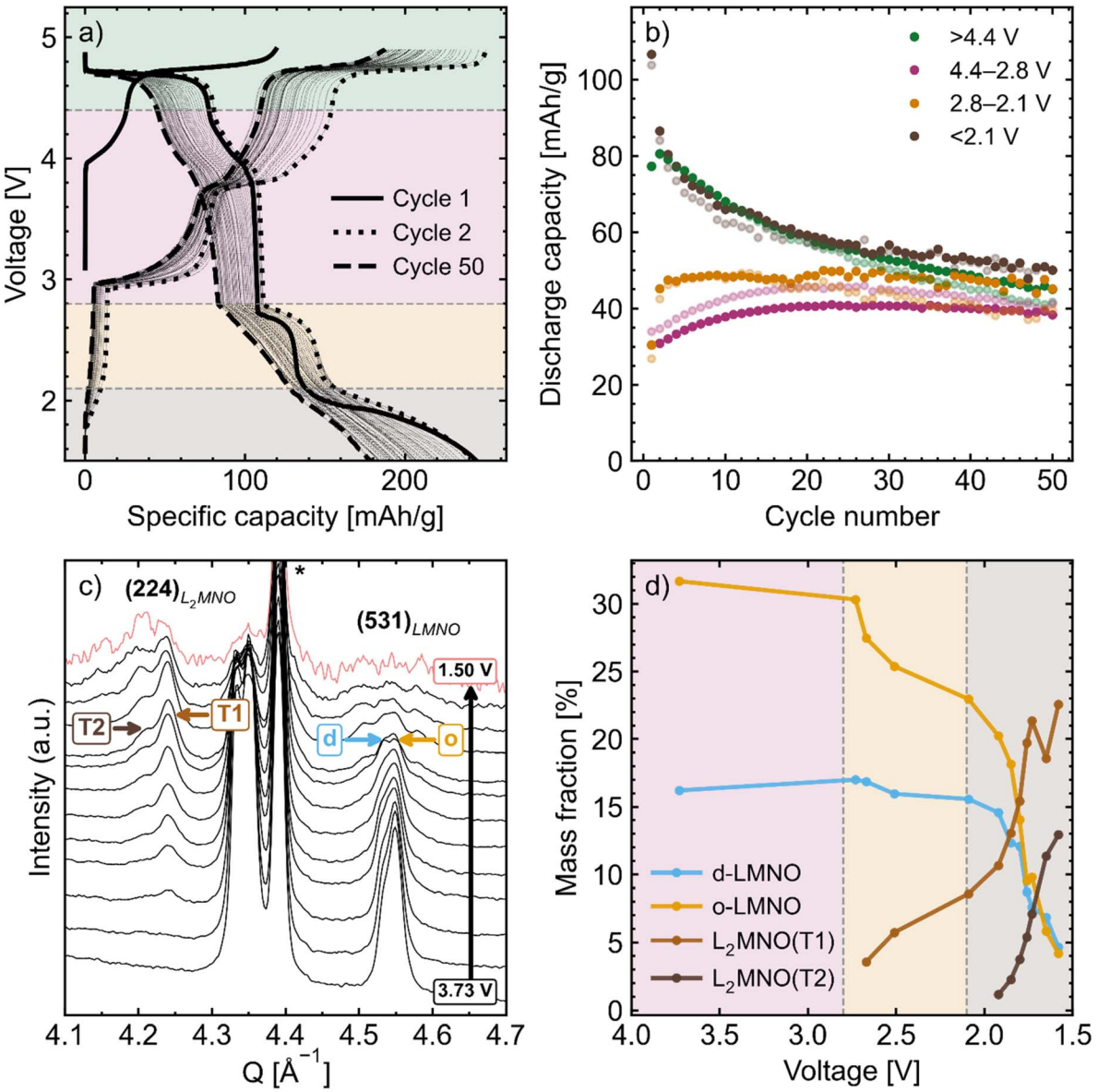

Fig. 14 (a) Galvanostatic cycling (C/8 in coin cell) of Mn1.6-500C-72 h in an extended voltage range (1.5–5.0 V), highlighting the first, second and 50th cycle. Experimental details are written in Table S11. The background colors mark the voltage ranges used for further calculations: (b) calculated specific discharge capacity contribution from different voltage ranges relevant to the galvanostatic cycling of Mn1.6-500C-72 h, over the full 50 cycles. A parallel sample shows reproducible data plotted as a shadow. (c) *Operando* SXRD data of Mn1.6-500C-72 h from the first deep discharge (C/8 in *operando* cell), from 4 V (bottom) to 1.5 V (top). As voltage lowers, LMNO peaks disappear [see (531)-reflection of d- and o-LMNO] and two tetragonal phases, L_2MNO (T1) and $L_{2.5}$MNO (T2), arise. The dominant peak (*) represents the Al current collector. The final diffractogram in pink color was not used in the Rietveld refinement, as explained in the caption of Fig. S33. (d) Rietveld refined mass fractions from the diffractograms in (c), illustrating how o-LMNO and d-LMNO are transforming into the two Li-rich tetragonal phases. Plotted without errors for improved readability, see Fig. S34 for included error bars.

of Ni remain largely unchanged throughout this voltage region, which implies that the low voltage activity is driven by Mn-redox. Coin cell data in Fig. 14a and b show that the activity from Ni is gradually altered and contributes significantly to the overall capacity fading. The correlation of T1 with o-LMNO and T2 with d-LMNO, as well as the prominent electrochemical fading in the low voltage regime, suggests that the insertion of excess Li is more reversible for o-LMNO than for (in our case; Mn-rich) d-LMNO – in line with previous reports.[17,84]

Discussion

The excellent signal-to-noise ratio for the synchrotron data along with high angular resolution enables disclosure of features that otherwise are partly hidden in background or peak profiles, related to phase coexistence, cation-ordering and segregation. The various phases in the Li–Mn–Ni–O multicomponent system have their distinct characteristics that facilitate the analysis. The current quantitative approach was evaluated

by comparing the calculated average chemical composition based on refined phase fractions, lattice parameters and cation site occupancies with nominal composition. Since X-rays have limitations regarding Mn/Ni scattering contrast and scattering from light elements, it would be beneficial if powder XRD and neutron diffraction could be combined, taking advantage of the scattering contrast provided by neutrons and the peak resolution by X-rays. We see this as a preferred route for analysis of multicomponent materials where slight compositional variations may impact technological (electrochemical) performance. The complexity arises from substantial cation mobility at temperatures as low as 400–500 °C, which is governed by the large number of available tetrahedral and octahedral sites. In an energy landscape perspective, the way of site filling in the O-ccp gives rise to many well-defined structure types, see Fig. 15. However, there may exist intermediate (metastable) situations that also are low in total energy. Hence, at the local scale restructuring is feasible and dynamic.

Since the Mn-rich samples show clear splitting into more spinel phases, it is tempting to suggest that this is the case also for the stoichiometric Mn1.5-samples, but to a much lesser extent. We observe that *e.g.* Mn1.5-O2-700C has ~2 wt% o-RS. Assuming eqn (4) holds, the o-RS in this sample has composition $Li_{0.74}Ni_{5.63}MnO_6$ and the resulting average spinel must be Mn-rich (Mn/Ni ratio of 3.2, ~$LiMn_{1.53}Ni_{0.47}O_4$) to maintain the overall Mn/Ni ratio of 3.0 for the bulk as confirmed by ICP-OES. This would explain why presumably stoichiometric LMNO in practice always show $Mn^{3+/4+}$ electrochemical activity.[64]

The initial high-temperature calcination (800–900 °C) provides substantial amounts of o-RS and N-layered impurities, up to 6 wt% and 4 wt%, respectively. These Ni-rich impurities reduce the energy capacity of the cathode material and are thus unwanted. Based on *ex situ* data for annealed samples, we identified the conditions where these impurities back-transform into LMNO. The N-layered impurity transforms to spinel for in the range 500–725 °C, whereas the o-RS impurity is most efficiently removed at around 650 °C in air, and even more effectively at 700 °C in O_2-flow. In general, higher pO_2 and more Mn-rich samples, leads to both (i) less o-RS and (ii) less Li-rich composition (based on the proposed lattice parameter-stoichiometry relation, eqn (4)). The Mn-rich samples back-transform most of their Ni-rich impurities already at low annealing temperatures (~500 °C), most effectively in O_2-rich atmosphere. The experimental snapshots after 6 h of annealing do not represent a final stage, for that prolonged annealing is necessary, as for the MO-samples. Restructuring continues for extended times, and this also applies to the cation ordering. For the Mn-rich samples the temperature range where o-RS is most effectively removed coincides with the range where Mn/Ni cation ordering is fast.[64] Hence, the mechanisms for impurity formation and ordering appear to be linked. When the octahedral 16c sites in the spinel (oxygen ccp) are filled (as is the case for o-RS), they become a hindrance that disrupts the cation ordering process in LMNO.[86]

The o-RS precipitate has Mn and Ni in the same oxidation states as in the parent o-LMNO phase. However, the removal of a relative high fraction of Ni(II) from the octahedral voids of the

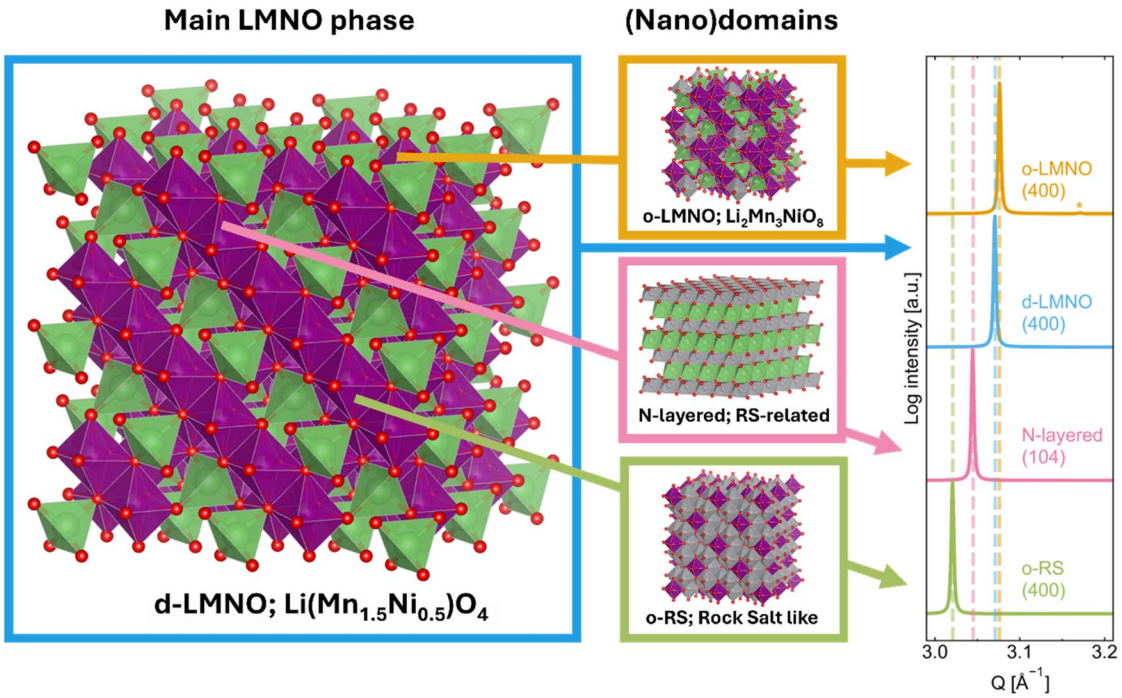

Fig. 15 Illustration of the complexity of the phases that can be present in LMNO-materials. What can look like phase pure d-LMNO might very well have domains of other phases, *e.g.* partially ordered o-LMNO or impurities such as N-layered or ordered rock salt-structures. The phases are hard to separate in diffractograms, especially as the spinel phase peaks tend to be rather broad and dominant, unless impurities as present in large amounts or are measured with very high-resolution diffraction.

spinel may have a significant effect on the stability of the oxygen anions in the spinel that bonds to 1 Li, 2 Mn and 1 Ni in the ideal o-LMNO case. Considering a local O–$LiMn_2Ni$ tetrahedron, this O-anion will experience a too high positive charge if one Ni(II) is replaced by Mn(IV). At least two options then appear; (i) incorporation of some Li(I) in octahedral sites, or (ii) a reduction of manganese. The latter case will in turn trigger oxygen release. Hence, it is plausible that the o-RS precipitation triggers a restructuring and reduction of the Mn-spinel cations, which is a likely cause for the reported O_2 release:

$$LiMn_{1.5}Ni_{0.5}O_4 \Leftrightarrow nLiMn_{1.5+x}Ni_{0.5-x}O_4 + mMn[Li_zNi_{6-z}][Li_z]O_8 + \frac{n \times x}{2}O_2 \quad (6)$$

According to McCalla *et al.* no RS phase exists for the nominal stoichiometry $LiMn_{1.5}Ni_{0.50}O_4$ at 800 °C.[41] This represents the ideal (equilibrium) situation. In real samples, the compositional fluctuations and the dynamics of the synthesis, provide an energy landscape with 4–5 potentially co-existing phases, as a metastable mix. The properties of an LMNO batch are not only dependent on the synthesis route, cooling procedure, atmosphere, and post annealing, but also on holding time/conditions at low temperatures.

The current analysis indicates the presence of spinel crystallites with a surplus of Mn in tetrahedral voids. The Bragg-reflections of this relevant e-LMNO-phase are unusually broad, which make detection and analysis more difficult. However, the broadening can be attributed to strain and is thus indicative of local variations in the Mn content in the tetrahedral voids. The identification of Mn-enriched e-LMNO has earlier for the most part escaped detection, though with exceptions.[50] For the mass balance calculations based on Rietveld refinements, it turned essential to incorporate e-LMNO. We note that e-LMNO is only present after low annealing temperatures and with Mn at Li-site only in the samples where also o-LMNO is present, see eqn (7). Its formation is probably linked to cation relocations as a response to local charge neutrality. Due to the complex phase relations, no balanced equation can be feasibly presented:

$$LiMn_{1.5+x}Ni_{0.5-x}O_4 \Leftrightarrow LiMn_{1.5}Ni_{0.5}O_4\ (o) + [Li_{1-y}Mn_y]Mn_{1.5+x'}Ni_{0.5-x'}O_4\ (e) \quad (7)$$

There is consensus in literature that d-LMNO shows the best electrochemical performance, although some reports suggest that a combination of d-LMNO and o-LMNO is superior.[87] In such evaluations, a correct structural analysis is obviously required, which could present challenges. As means to evaluate the status with respect to Mn/Ni ordering, we recommend the concept of relative order (RO), and to make comparisons based on integrated intensities of Bragg reflections that are sensitive to Mn/Ni ordering and its related atomic displacements. A major drawback is that synchrotron radiation data appears to be required. However, very recently we proved that a top-end rotating anode system with 2D detector can provide the required basic data (Fig. S35). This could broaden the use of RO as a facile structural parameter. SXRD and Raman spectroscopy provide complementary insights into the ordering process, particulary regarding the size of the ordered domains, and to early stages of nucleation and growth. Raman spectroscopy is indeed a facile tool for distinguishing o- and d-LMNO, given that due attention is paid to impurities.

In this work we observe Mn/Ni ordering already around 400–450 °C. To our knowledge, such low ordering temperatures have not been reported previously for LMNO, except for in partly delithiated samples.[74] This is interesting, as Frenkel defects are not expected to occur below 500 °C for stoichiometric $LiMn_{1.5}Ni_{0.5}O_4$.[45] The lack of such earlier findings could be due to challenges in characterization, since there is currently no doubt that Mn/Ni ordering, locally and globally, occurs already at 400–450 °C, in particular for Mn-enriched samples.

The literature reports a large spread in the lattice parameters of stoichiometric $LiMn_{1.5}Ni_{0.5}O_4$, not only for d-LMNO,[41] but also for the ordered variant. Several reports suggest that this is due to varying Mn(III)-amounts in LMNO, and further argue that this correlates with oxygen vacancies. The current work rather provides support for claiming that the change in lattice parameters, is directly connected to the o-RS and N-layered precipitation reactions, and consequent compositional changes in the spinel. The changes with respect to annealing temperature then reflects partial back-transformation of o-RS and N-layered phases to an LMNO spinel with slightly modified composition.

The Mn-rich LMNO samples, with an Mn/Ni ratio above three, will contain Mn(III) given full Li occupancy and no O-vacancies. The presence of electroactive Mn(III) is easily confirmed and quantified from galvanostatic cycling data. Fig. 16 shows the variation in the *a*-axis for o-LMNO for various nominal compositions and annealing temperatures. A pertinent question is how this variation can be understood. One may envisage that the Mn(III) Jahn–Teller active d^4-ion is slightly destabilized in its deformed octahedral environment.

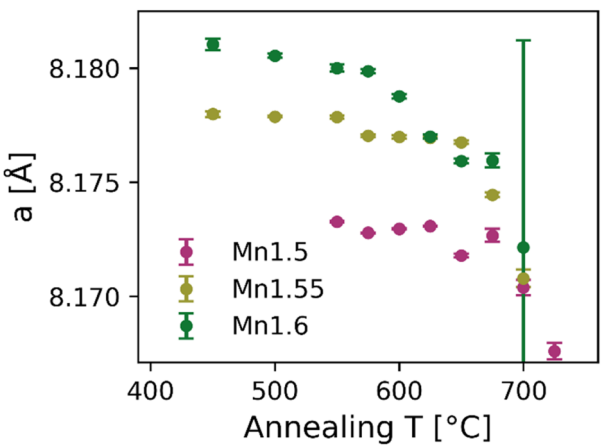

Fig. 16 Lattice parameter development of the o-LMNO phase in samples heated in O_2-flow, showing a clear decreasing trend for higher annealing temperatures.

Alternatively, one may envisage a charge disproportionation: 2Mn(III) → Mn(II) and Mn(IV) where Mn(IV) is stabilized with a local structure corresponding to that in $Li_2Mn_3NiO_8$ whereas Mn(II) enters a tetrahedral site (partly exchanged with Li). In this way Mn(IV) acts as a driving force for local ordering and favourable Mn–O–Ni bonding. This driving force remains in Mn-rich samples and may explain why ordering occurs at low temperatures for such samples. Furthermore, the current observation of the third spinel phase (e-LMNO), enriched in Mn at the tetrahedral sites, aligns with this hypothesis. Notably, e-LMNO is only detected at the lowest annealing temperatures, *i.e.* below 500–550 °C for Mn1.6 and below 600–625 °C for Mn1.55, which correlates well with the observation of o-LMNO in these samples. The link between e-LMNO and o-LMNO is even clearer when considering Mn1.55-400C. This is the only Mn1.55-sample heated below 725 °C that shows no signs of cation ordering. For this sample there is no clear sign of Mn in the 8a-site of e-LMNO as opposed to the situation for ordered Mn-rich samples heated at similar conditions (450/500 °C in air/O_2). Since tiny, ordered domains will easily escape SXRD detection, Raman stands out as the key tool for characterizing LMNO with very small ordered domains (as is the case in low temperature ordering), and subsequently for correlating them with electrochemical performance. This ought to be given weight in future works.

We believe that the two characterization techniques used in this work, along with the fact that we are using a wet chemical synthesis approach, is crucial for identifying low temperature ordering. The route enables atomic mixing, and localized order can be detected by Raman in cases where additional peaks and splitting are hardly identified by SXRD. It is clear that the Mn/Ni-ratio of a given sample affects the ordering properties. For the current samples we observed from post mortem analyses by Raman that cation order can be enhanced by electrochemical cycling itself. However, further studies are needed.

The thermal stability of o-LMNO in Mn1.5, Mn1.55 and Mn1.6 differs significantly (Fig. 11a–c). For Mn1.5, the RO increases with holding temperature up to 725 °C in O_2, after which the spinel partly decomposes and changes composition. For Mn1.55 the RO increases for annealing up to around 575 °C, and above this it gradually decreases. Notably, Raman still sees the Mn1.55-700C as very ordered (Fig. 13), despite being predominantly disordered at the length scale of diffraction (Fig. S14). Hence, the apparent disordered state could rather represent a situation with nanosized ordered domains in a disordered matrix. This could also be the case for Mn1.6, where RO decreases for annealing temperatures above 450 °C. Possibly, the lowered stability of o-LMNO in Mn1.55 and Mn1.6 reflects an increased Mn(III) content that reduces the energy gain for the chemical bonding between small Mn(IV) and large Ni(II) cations.

Even for MO-samples, subjected to very slow cooling, a slight broadening occurs for the superstructure peaks relative to the spinel main peaks. This reflects the smaller size of ordered domains that nucleate randomly and grow until they encounter a separate domain with a non-matching Mn/Ni distribution, forming an anti-phase boundary (APB), which in turn limits the domain size. This is in line with reports claiming that 48 hours annealing still gives peak broadening[6] and that a large number of APBs are present at equilibrium.[15]

Electrochemical data provides an independent supplement to the SXRD data for validating the Mn/Ni-ratio. Stüble *et al.* used such data to determine the Mn/Ni-stoichiometry of the spinel.[64] In principle, this represents a more accurate description beyond just reporting the bulk stoichiometry. It is, however, not an ideal way to characterize the pristine material, as side reactions are occurring, especially at high voltages where the electrolyte is outside its stability window. Furthermore, various impurity phases may contribute electrochemically. It is noteworthy that reported capacities, here and in the literature, are significantly lower than the theoretical values. Hence, the electrochemical data do not fully describe the entire sample, but rather just the electrochemically active parts.[82] In this respect, SXRD can help identifying the reason for reduced electrochemical activity. The current *operando* data shows that o-LMNO and d-LMNO can be distinguished during cycling. However, this is not feasible for all relevant Mn/Ni stoichiometries during conventional cycling (3–5 V) owing to major peak overlap between relevant phases (*i.e.* $LiMn_{1.5+x}Ni_{0.5-x}O_4$, $Li_{0.5}Mn_{1.5+x}Ni_{0.5-x}O_4$ and $Mn_{1.5+x}Ni_{0.5-x}O_4$ in ordered and disordered variants). However, *operando* SXRD is suitable to study the behavior at the very low potentials, as the tetragonally distorted Li-rich phases (T1 and T2) are easily distinguishable and can be correlated with the degradation of o-LMNO and d-LMNO. This process can successfully be studied *operando*, whereas any post mortem studies are unsuited as T2 transforms into T1 after short resting times.[17] Our findings suggest that the low voltage behavior should be further investigated, to improve structural insight, to become able to distinguish the phases electrochemically, and to improve the knowledge basis for making prelithiated LMNO a viable option in future batteries.

A note with respect to capacity fading is that even if the initial phase composition is known, it remains open how phase fractions may change during charge/discharge. As these are long term processes, often with very subtle changes from one cycle to the next, post mortem studies of aged cells should be prioritized over *operando* studies, at least for cycling in the conventional voltage range. That is also the case when studying the finer structural details that are highlighted in the current work, as *operando* studies may fail to properly identify such details.

Conclusions

We have explored stability and structural aspects of three categories of LMNO materials that in sum are representative as realistic electrode materials, based on detailed characterization using synchrotron powder X-ray diffraction and Raman spectroscopy. The work benchmarks how structural properties depend on processing conditions and how insight is achieved by means of sharp characterization methods.

Five different phases are observed in these samples, with coexistence of up to four phases identified in snapshots from different stages of synthesis and processing. We observe that

Mn/Ni cation diffusion takes place at much lower temperatures than earlier anticipated, as evidenced by progressing Mn/Ni cation ordering in LMNO and (back)formation of rock salt and N-layered impurity phases. As a response to this as well as cation ordering and restructuring of the spinel phase(s), a distinct e-LMNO spinel impurity with excess Mn/Ni in tetrahedral sites is formed during low-temperature annealing of quenched samples. All these processes are drivers for formation of Mn(III) as recognized by galvanostatic cycling, thus providing highly valuable input to composition-property correlations for LMNO.

The excellent SXRD data document peak broadening, peak shoulders and weak diffraction peaks. Based on such observations we identify and describe size and growth/stability of ordered domains of o-LMNO in co-existence with d-LMNO and determine lattice parameters as function of composition and processing parameters. We note that o-RS reactivity and Mn/Ni ordering occur within the same temperature window and conclude that the formation of o-RS triggers an oxygen release without formation of O-vacancies in the parent spinel.

The quantitative Rietveld analysis of the multi-phased samples fully reproduced the nominal composition of the bulk material. The analysis benefited from correlations between composition and lattice parameters for the different LMNO-phases. We conclude that a proper analysis of any LMNO materials should include the o-RS phase and should not assume the phase purity of LMNO. In terms of validating the proposed lattice parameter-composition relations in this work, the poor scattering contrast of X-rays should be compensated for by conducting a combined X-ray and neutron diffraction experiment in future works. We point out that *operando* studies can distinguish o-LMNO and d-LMNO for certain compositions, however, the o-RS phase is often present in too small amounts to be observed owing to a moderate signal-to-noise ratio. On the other hand, the transformations into tetragonal LMNO variants at low voltages are easily investigated.

We deliberately made large batches and subsequently treated small-scale samples differently. Although the Mn/Ni distribution is homogeneous in the gel after drying, subsequent (Pechini) combustion may affect nucleation in the large batch. Possibly, even more homogeneous batches can be achieved. The current goal was to mimic materials likely to be synthesized and studied in various laboratories, relevant also for scaling up production capabilities. Impurities and inhomogeneities are then unavoidable, and one should know how this may unfold – especially if LMNO is to be produced at the massive scale needed to be industrially relevant.

The recommended synthesis route based on our findings is thus a soft chemical synthesis approach to enforce a homogenous cation distribution. Lowering the calcination temperature to some 700–800 °C and shorter durations (<20 h) are also expected to have a positive impact (less impurity formation, see eqn (6)). Based on our findings we recommend having a Mn-enriched sample to avoid trapping of active Ni in impurity phases. Annealing under O_2-flow around 500 °C appears efficient for removing of any impurities (o-RS/N-layered) for these samples. In our work, 6 hours were used; however, less time is likely sufficient – especially for samples with a softer calcination step. Our work shows that holding time – even at low temperatures (see eqn (7)) during *e.g.* cooling – is an essential processing parameter to consider and must be optimized. Even at 500 °C Mn-rich samples undergo ordering (and can even form e-LMNO, having an unknown electrochemical effect), so finding the perfect compromise remains a challenge.

Author contributions

All experimental work, data analysis and drafting of manuscript done by Halvor Høen Hval. The role of Helmer Fjellvåg has been supervision throughout the project, as well as being active in the writing of the manuscript.

Conflicts of interest

There are no conflicts to declare.

Data availability

The data that support the findings of this study are available from the corresponding author upon reasonable request.

Supplementary information is available. See DOI: **https://doi.org/10.1039/d5ta05130d**.

Acknowledgements

We acknowledge funding through MoZEES, a Norwegian Centre for Environment-friendly Energy Research (FME), co-sponsored by the Research Council of Norway (project number 257653) and 40 partners from research, industry, and public sector. The authors express gratitude for being granted synchrotron beamtime at SNBL (ESRF) and for the valuable assistance provided by the SNBL staff prior to, during and after the experiments. In particular we would like to thank Vadim Dyadkin, Dmitry Chernyshov and Charlie McMonagle from BM01 and Kenneth Marshall from BM31. Rasmus Vester Thøgersen (UiO) is also thanked for his contributions in planning, execution and analysis of the *operando* experiments. Data collection at RECX, the Norwegian Center for X-ray diffraction and scattering (Research Council of Norway, project 208896) is also acknowledged. Thank you also to the Organic Surface Chemistry group at Aarhus University (AU) and Marcel Ceccato (AU) for access to the Raman Spectrometer. Chris Erik Mohn (UiO) is furthermore thanked for DFT-work and great discussions along the way.

Notes and references

1 A. Manthiram, K. Chemelewski and E.-S. Lee, *Energy Environ. Sci.*, 2014, 7, 1339–1350.
2 W. Li, B. Song and A. Manthiram, *Chem. Soc. Rev.*, 2017, **46**, 3006–3059.
3 M. S. Whittingham, *Chem. Rev.*, 2004, **104**, 4271–4301.
4 M. Armand, P. Axmann, D. Bresser, M. Copley, K. Edström, C. Ekberg, D. Guyomard, B. Lestriez, P. Novák,

M. Petranikova, W. Porcher, S. Trabesinger, M. Wohlfahrt-Mehrens and H. Zhang, *J. Power Sources*, 2020, **479**, 228708.
5 H. Duncan, B. Hai, M. Leskes, C. P. Grey and G. Chen, *Chem. Mater.*, 2014, **26**, 5374–5382.
6 J. Kim, A. Huq, M. Chi, N. P. W. Pieczonka, E. Lee, C. A. Bridges, M. M. Tessema, A. Manthiram, K. A. Persson and B. R. Powell, *Chem. Mater.*, 2014, **26**, 4377–4386.
7 K. Lee, G. J. Yang and Y. Kim, *Ceram. Int.*, 2017, **43**, 15510–15518.
8 M. Kunduraci and G. G. Amatucci, *J. Power Sources*, 2007, **165**, 359–367.
9 B. Aktekin, M. Valvo, R. I. Smith, M. H. Sørby, F. L. Marzano, W. Zipprich, D. Brandell, K. Edström and W. R. Brant, *ACS Appl. Energy Mater.*, 2019, **2**, 3323–3335.
10 Y. Chen and K. An, *J. Energy Chem.*, 2022, **68**, 60–70.
11 S. Liu, X. Chen, J. Zhao, J. Su, C. Zhang, T. Huang, J. Wu and A. Yu, *J. Power Sources*, 2018, **374**, 149–157.
12 Z. Moorhead-Rosenberg, A. Huq, J. B. Goodenough and A. Manthiram, *Chem. Mater.*, 2015, **27**, 6934–6945.
13 J. Song, D. W. Shin, Y. Lu, C. D. Amos, A. Manthiram and J. B. Goodenough, *Chem. Mater.*, 2012, **24**, 3101–3109.
14 N. Emery, A. Bhatia, Y. Ghaleb, A. O. Mitrushchenkov, C. Léonard, J. P. Pereira-Ramos, R. Baddour-Hadjean and R. I. Smith, *Chem. Mater.*, 2022, **34**, 3152–3167.
15 M. Casas-Cabanas, C. Kim, J. Rodríguez-Carvajal and J. Cabana, *J. Mater. Chem. A*, 2016, **4**, 8255–8262.
16 J. Liu, A. Huq, Z. Moorhead-Rosenberg, A. Manthiram and K. Page, *Chem. Mater.*, 2016, **28**, 6817–6821.
17 E. Lee, K. Nam, E. Hu and A. Manthiram, *Chem. Mater.*, 2012, **24**, 3610–3620.
18 L. Wang, H. Li, X. Huang and E. Baudrin, *Solid State Ionics*, 2011, **193**, 32–38.
19 J.-H. Kim, S.-T. Myung, C. S. Yoon, S. G. Kang and Y.-K. Sun, *Chem. Mater.*, 2004, **16**, 906–914.
20 E. Lee and K. A. Persson, *Chem. Mater.*, 2013, **25**, 2885–2889.
21 P. B. Samarasingha, J. Sottmann, S. Margadonna, H. Emerich, O. Nilsen and H. Fjellvåg, *Acta Mater.*, 2016, **116**, 290–297.
22 A. Bhatia, Y. D. Zrelli, J. P. Pereira-Ramos and R. Baddour-Hadjean, *J. Mater. Chem. A*, 2021, **9**, 13496–13505.
23 H. Komatsu, H. Arai, Y. Koyama, K. Sato, T. Kato, R. Yoshida, H. Murayama, I. Takahashi, Y. Orikasa, K. Fukuda, T. Hirayama, Y. Ikuhara, Y. Ukyo, Y. Uchimoto and Z. Ogumi, *Adv. Energy Mater.*, 2015, **5**, 1500638.
24 M. Lin, L. Ben, Y. Sun, H. Wang, Z. Yang, L. Gu, X. Yu, X. Yang, H. Zhao, R. Yu, M. Armand and X. Huang, *Chem. Mater.*, 2015, **27**, 292–303.
25 B. Aktekin, F. Massel, M. Ahmadi, M. Valvo, M. Hahlin, W. Zipprich, F. Marzano, L. Duda, R. Younesi, K. Edström and D. Brandell, *ACS Appl. Energy Mater.*, 2020, **3**, 6001–6013.
26 J. Zheng, J. Xiao, X. Yu, L. Kovarik, M. Gu, F. Omenya, X. Chen, X.-Q. Yang, J. Liu, G. L. Graff, M. S. Whittingham and J.-G. Zhang, *Phys. Chem. Chem. Phys.*, 2012, **14**, 13515–13521.
27 M. Kunduraci, J. F. Al-Sharab and G. G. Amatucci, *Chem. Mater.*, 2006, **18**, 3585–3592.
28 J. Xiao, X. Chen, P. V. Sushko, M. L. Sushko, L. Kovarik, J. Feng, Z. Deng, J. Zheng, G. L. Graff, Z. Nie, D. Choi, J. Liu, J.-G. Zhang and M. S. Whittingham, *Adv. Mater.*, 2012, **24**, 2109–2116.
29 R. Amin and I. Belharouak, *J. Power Sources*, 2017, **348**, 311–317.
30 J. Yoon, D. Kim, J. H. Um, M. Jeong, W. Oh and W. S. Yoon, *J. Alloys Compd.*, 2016, **686**, 593–600.
31 H. Ryoo, S.-G. Lee, J.-G. Kim and S.-Y. Chung, *Adv. Funct. Mater.*, 2019, **29**, 1805972.
32 J. Cen, B. Zhu, S. R. Kavanagh, A. G. Squires and D. O. Scanlon, *J. Mater. Chem. A*, 2023, **11**, 13353–13370.
33 D. Pasero, N. Reeves, V. Pralong and A. R. West, *J. Electrochem. Soc.*, 2008, **155**, A282.
34 Y. Chen, Y. Sun and X. Huang, *Comput. Mater. Sci.*, 2016, **115**, 109–116.
35 J. Cabana, M. Casas-Cabanas, F. O. Omenya, N. A. Chernova, D. Zeng, M. S. Whittingham and C. P. Grey, *Chem. Mater.*, 2012, **24**, 2952–2964.
36 L. Cai, Z. Liu, K. An and C. Liang, *J. Mater. Chem. A*, 2013, **1**, 6908–6914.
37 L. Boulet-Roblin, D. Sheptyakov, P. Borel, C. Tessier, P. Novák and C. Villevieille, *J. Mater. Chem. A*, 2017, **5**, 25574–25582.
38 M. Fehse, N. Etxebarria, L. Otaegui, M. Cabello, S. Martín-Fuentes, M. A. Cabañero, I. Monterrubio, C. F. Elkjær, O. Fabelo, N. A. Enkubari, J. M. L. Del Amo, M. Casas-Cabanas and M. Reynaud, *Chem. Mater.*, 2022, **34**, 6529–6540.
39 Q. Zhong, A. Bonakdarpour, M. Zhang, Y. Gao and J. R. Dahn, *J. Electrochem. Soc.*, 1997, **144**, 205–213.
40 D. Lu, M. Xu, L. Zhou, A. Garsuch and B. L. Lucht, *J. Electrochem. Soc.*, 2013, **160**, A3138.
41 E. McCalla and J. R. Dahn, *Solid State Ionics*, 2013, **242**, 1–9.
42 W. Bronger, H. Bade and W. Klemm, *Z. Anorg. Allg. Chem.*, 1964, **333**, 188–200.
43 P. B. Samarasingha, N. H. Andersen, M. H. Sørby, S. Kumar, O. Nilsen and H. Fjellvåg, *Solid State Ionics*, 2016, **284**, 28–36.
44 L. Boulet-Roblin, C. Villevieille, P. Borel, C. Tessier, P. Novák and M. Ben Yahia, *J. Phys. Chem. C*, 2016, **120**, 16377–16382.
45 H. Ryoo, H. B. Bae, Y. M. Kim, J. G. Kim, S. Lee and S. Y. Chung, *Angew. Chem., Int. Ed.*, 2015, **54**, 7963–7967.
46 G. B. Zhong, Y. Y. Wang, X. J. Zhao, Q. S. Wang, Y. Yu and C. H. Chen, *J. Power Sources*, 2012, **216**, 368–375.
47 G. Liu, J. Zhang, X. Zhang, Y. Du, K. Zhang, G. Li, H. Yu, C. Li, Z. Li, Q. Sun and L. Wen, *J. Alloys Compd.*, 2017, **725**, 580–586.
48 D. W. Shin, C. A. Bridges, A. Huq, M. P. Paranthaman and A. Manthiram, *Chem. Mater.*, 2012, **24**, 3720–3731.
49 J. Zeng, K. Wu, N. Li, L. He, B. Wang, X. Lin and E. Zhao, *ACS Appl. Energy Mater.*, 2024, **7**, 2405–2415.
50 F. A. Vásquez, N. C. Rosero-Navarro, A. Miura, R. Jalem, Y. Goto, M. Nagao, Y. Tateyama, K. Tadanaga and J. A. Calderón, *ACS Appl. Mater. Interfaces*, 2021, **13**, 14056–14067.
51 Y. Chen, Y. Cheng, J. Li, M. Feygenson, W. T. Heller, C. Liang and K. An, *Adv. Energy Mater.*, 2017, **7**, 1601950.

52 W. Liu, G. C. Farrington, F. Chaput and B. Dunn, *J. Electrochem. Soc.*, 1996, **143**, 879–884.
53 V. Dyadkin, P. Pattison, V. Dmitriev and D. Chernyshov, *J. Synchrotron Radiat.*, 2016, **23**, 825–829.
54 D. Chernyshov, V. Dyadkin, H. Emerich, G. Valkovskiy, C. J. McMonagle and W. van Beek, *Acta Crystallogr.*, 2021, **A77**, 497–505.
55 R. V. Thøgersen, H. H. Hval and H. Fjellvåg, *Batteries Supercaps*, 2024, **7**, e202400348.
56 E. McCalla, A. W. Rowe, R. Shunmugasundaram and J. R. Dahn, *Chem. Mater.*, 2013, **25**, 989–999.
57 N. M. Jobst, N. Paul, P. Beran, M. Mancini, R. Gilles, M. Wohlfahrt-Mehrens and P. Axmann, *J. Am. Chem. Soc.*, 2023, **145**, 4450–4461.
58 O. C. Gagné and F. C. Hawthorne, *IUCrJ*, 2020, **7**, 581–629.
59 M. Wenger and T. Armbruster, *Eur. J. Mineral.*, 1991, **3**, 387–399.
60 J. F. Bérar and P. Lelann, *J. Appl. Crystallogr.*, 1991, **24**, 1–5.
61 N. M. Hagh and G. G. Amatucci, *J. Power Sources*, 2014, **256**, 457–469.
62 G. H. Carey and J. R. Dahn, *ACS Comb. Sci.*, 2011, **13**, 186–189.
63 H. Berg, J. O. Thomas, W. Liu and G. C. Farrington, *Solid State Ionics*, 1998, **112**, 165–168.
64 P. Stüble, V. Mereacre, H. Geßwein and J. R. Binder, *Adv. Energy Mater.*, 2023, **13**, 2203778.
65 H. Taguchi, *Solid State Commun.*, 1998, **108**, 635–639.
66 J. M. Tarascon, W. R. McKinnon, F. Coowar, T. N. Bowmer, G. Amatucci and D. Guyomard, *J. Electrochem. Soc.*, 1994, **141**, 1421–1431.
67 Y.-J. Gu, Y. Li, Y.-B. Chen and H.-Q. Liu, *Electrochim. Acta*, 2016, **213**, 368–374.
68 A. Feltz, J. Töpfer and B. Neidnicht, *Z. Anorg. Allg. Chem.*, 1993, **619**, 39–46.
69 J. S. Kasper and J. S. Prener, *Acta Crystallogr.*, 1954, **7**, 246–248.
70 A. W. Rowe, PhD dissertation, Dalhousie University, 2014.
71 W. D. Johnston, R. C. Miller and R. Mazelsky, *J. Phys. Chem.*, 1959, **63**, 198–202.
72 H. H. Hval, H. Fjellvåg and C. E. Mohn, *Cation disordering, impurity segregation, and structure–composition relations in LMNO spinel revealed by high-resolution X-ray diffraction and ab initio simulations*, 2026.
73 H. Taguchi, S. Omori and M. Nagao, *J. Solid State Chem.*, 1995, **118**, 112–116.
74 O. Gustafsson, J. Kullgren and W. R. Brant, *ACS Appl. Energy Mater.*, 2023, **6**, 5000–5008.
75 C. M. Julien and A. Mauger, *AIMS Mater. Sci.*, 2018, **5**, 650–698.
76 N. Amdouni, K. Zaghib, F. Gendron, A. Mauger and C. M. Julien, *J. Magn. Magn. Mater.*, 2007, **309**, 100–105.
77 K. Dokko, M. Mohamedi, N. Anzue, T. Itoh and I. Uchida, *J. Mater. Chem.*, 2002, **12**, 3688–3693.
78 N. Mironova-Ulmane, A. Kuzmin, I. Steins, J. Grabis, I. Sildos and M. Pärs, *J. Phys.: Conf. Ser.*, 2007, **93**, 012039.
79 J.-X. Huang, B. Li, B. Liu, B.-J. Liu, J.-B. Zhao and B. Ren, *J. Power Sources*, 2016, **310**, 85–90.
80 K. Miwa, *Phys. Rev. B*, 2018, **97**, 075143.
81 X. Liu, D. Li, Q. Mo, X. Guo, X. Yang, G. Chen and S. Zhong, *J. Alloys Compd.*, 2014, **609**, 54–59.
82 E. McCalla, A. W. Rowe, C. R. Brown, L. R. P. Hacquebard and J. R. Dahn, *J. Electrochem. Soc.*, 2013, **160**, A1134–A1138.
83 A. Smith, P. Stüble, L. Leuthner, A. Hofmann, F. Jeschull and L. Mereacre, *Batteries Supercaps*, 2023, **6**, e202300080.
84 S.-H. Park, S.-W. Oh, C.-S. Yoon, S.-T. Myung and Y.-K. Sun, *Electrochem. Solid State Lett.*, 2005, **8**, A163–A167.
85 O. A. Drozhzhin, I. V. Tereshchenko, H. Emerich, E. V. Antipov, A. M. Abakumov and D. Chernyshov, *J. Synchrotron Radiat.*, 2018, **25**, 468–472.
86 J. Lee, N. Dupre, M. Avdeev and B. Kang, *Sci. Rep.*, 2017, **7**, 6728.
87 F. A. Vásquez, J. E. Thomas and J. A. Calderón, *Solid State Ionics*, 2020, **345**, 115199.